Journal of Nanobiotechnology

https://doi.org/10.1186/s12951-026-04476-1

Article in Press

Machine learning-advanced hydrogel-based transcription-coupled positive-feedback CRISPR/Cas13a analysis for novel microRNA signatures in differential diagnosis of non-small cell lung cancer

Received: 6 February 2026

Accepted: 12 April 2026

Published online: 27 April 2026

Cite this article as: Zhang Y., Wang Y., Ma D. *et al.* Machine learning-advanced hydrogel-based transcription-coupled positive-feedback CRISPR/Cas13a analysis for novel microRNA signatures in differential diagnosis of non-small cell lung cancer. *J Nanobiotechnol* (2026). https://doi.org/10.1186/s12951-026-04476-1

Yi Zhang, Yuzhi Wang, Deyu Ma, Guangjun Xiao, Lin Feng, Jialiang Cai, Yuanjiu Xu, Yongjian Wang, Xiaoyu Liu, Jiangchuan Tian, Zhong Zuo, Jianhua Lan, Bo Shen & Shijia Ding

ARTICLE IN PRESS

We are providing an unedited version of this manuscript to give early access to its findings. Before final publication, the manuscript will undergo further editing. Please note there may be errors present which affect the content, and all legal disclaimers apply.

If this paper is publishing under a Transparent Peer Review model then Peer Review reports will publish with the final article.

© The Author(s) 2026. **Open Access** This article is licensed under a Creative Commons Attribution-NonCommercial-NoDerivatives 4.0 International License, which permits any non-commercial use, sharing, distribution and reproduction in any medium or format, as long as you give appropriate credit to the original author(s) and the source, provide a link to the Creative Commons licence, and indicate if you modified the licensed material. You do not have permission under this licence to share adapted material derived from this article or parts of it. The images or other third party material in this article are included in the article's Creative Commons licence, unless indicated otherwise in a credit line to the material. If material is not included in the article's Creative Commons licence and your intended use is not permitted by statutory regulation or exceeds the permitted use, you will need to obtain permission directly from the copyright holder. To view a copy of this licence, visit http://creativecommons.org/licenses/by-nc-nd/4.0/.

ARTICLE IN PRESS

Machine Learning-Advanced Hydrogel-Based Transcription-Coupled Positive-Feedback CRISPR/Cas13a Analysis for Novel MicroRNA Signatures in Differential Diagnosis of Non-Small Cell Lung Cancer

Yi Zhang[1,2,†], Yuzhi Wang[3,†], Deyu Ma[2,†], Guangjun Xiao[4,†], Lin Feng[2], Jialiang Cai[2], Yuanjiu Xu[1], Yongjian Wang[1], Xiaoyu Liu[1], Jiangchuan Tian[1], Zhong Zuo[5,*], Jianhua Lan[6,*], Bo Shen[7,*], Shijia Ding[2,*]

[1]Department of Laboratory Medicine, West China Hospital, Sichuan University Sichuan University West China Hospital Guang'an Hospital, Guang'an People's Hospital, Guang'an, 638000, Sichuan, PR China

[2]Key Laboratory of Clinical Laboratory Diagnostics (Ministry of Education), College of Laboratory Medicine, Chongqing Medical University, Chongqing, 400016, PR China

[3]Department of Laboratory Medicine, Deyang People's Hospital, Deyang, 618000, Sichuan, PR China

[4]Department of Clinical Laboratory, Suining Central Hospital, Suining, 629000, PR China

[5]Department of Cardiology, The First Affiliated Hospital of Chongqing Medical University, Chongqing Medical University, Chongqing, 400016, PR China

[6]Department of Urology, West China Hospital, Sichuan University Sichuan University West China Hospital Guang'an Hospital, Guang'an People's Hospital, Guang'an, 638000, Sichuan, PR China

[7]Department of Laboratory Medicine, Chongqing Traditional Chinese Medicine Hospital, Chongqing, 400021, PR China

*Corresponding author.

E-mail address: dingshijia@163.com and dingshijia@cqmu.edu.cn (S. Ding); shenboszy228@163.com (B. Shen); ljhdoctor@yeah.net (J. Lan); zzuo-cq@hotmail.com (Z. Zuo).

[†]These authors contributed equally to this work.

ARTICLE IN PRESS

ARTICLE IN PRESS

ABSTRACT

MicroRNAs (miRNAs) hold significant potential as biomarkers for the precise diagnosis of non-small cell lung cancer (NSCLC). However, miRNAs remain underused due to their low abundance, high heterogeneity, and complex matrix interference in liquid biopsies, as well as the requirement for specialized techniques. Herein, we devised a hydrogel-based transcription-coupled positive-feedback CRISPR/Cas13a (TCPFC) enhanced electrochemiluminescent (ECL) analyzer for advanced analysis of plasma miRNA signatures via machine learning (ML). Initially, three NSCLC-associated miRNA signatures (miR-203b, miR-450b, and miR-642a) were identified from plasma miRNA datasets and validated using RT-qPCR. An Au@ACZ-SA-PEG hydrogel emitter was engineered to deliver a robust ECL output on a glassy carbon electrode. Additionally, the TCPFC strategy utilized transcription-coupled positive-feedback CRISPR/Cas13a to achieve cascade signal amplification. Concurrently, collateral cleavage eliminated dopamine quenchers, thereby restoring the ECL signal ("OFF-ON") for readout and achieving attomolar-level detection. The integration of ML algorithms with the hydrogel-based TCPFC-ECL platform yielded differential diagnosis accuracies of 97.27% (train, n = 110) and 93.64% (validation, n = 110), effectively distinguishing healthy controls (HC) from patients with stages I/II and III/IV NSCLC. Consequently, this biosensing platform demonstrates considerable promise as a practical tool for the precise diagnosis of NSCLC.

Keywords: MicroRNA signatures, Non-small cell lung cancer, Hydrogels, Machine learning, Differential diagnosis

ARTICLE IN PRESS

ARTICLE IN PRESS

Introduction

Lung cancer stands as a paramount global health challenge, representing the leading cause of cancer-related mortality worldwide with an annual incidence of approximately 2.5 million cases and 1.8 million deaths [1]. The predominant subtype, non-small cell lung cancer (NSCLC), accounts for 80-90% of all diagnoses and is primarily comprised of lung adenocarcinoma (LUAD) and lung squamous cell carcinoma (LUSC) [2]. The critical importance of early and differential diagnosis in improving patient survival rates and treatment efficacy cannot be overstated [3,4]. Pathological tissue biopsy is the gold standard for diagnosing NSCLC, but this approach has inherent limitations, including a risk of false negatives related to lesion size and depth, and potential complications such as hemorrhage, tumor rupture, and dissemination, as well as invasive procedure leading to suboptimal patient compliance [5,6]. The advent of low-dose computed tomography (LDCT) has improved the early detection of pulmonary nodules [7,8], its effectiveness is constrained by a high rate of false-positive results, resulting in unnecessary radiative follow-up procedures and substantial financial burden [9,10]. Consequently, these constraints highlight a pressing need for an approach capable of accurately identifying NSCLC in early and differential diagnosis.

Liquid biopsies present significant opportunities in precision oncology by delivering dynamic molecular insights into the entire tumor through minimally invasive and repeatable analysis [11,12]. In clinical practice, protein biomarkers like carcinoembryonic antigen (CEA), squamous cell carcinoma antigen (SCCA), and cytokeratin-19 fragments (CYFRA21-1) are less invasive but exhibit limited sensitivity for monitoring NSCLC [13]. MiRNAs are short non-coding RNAs that circulate in blood in a remarkably stable form, often packaged in extracellular vesicles or bound to argonaute proteins [14]. This stability, together with their defined sequences, has made them promising non-invasive biomarkers for monitoring of diseases [15,16]. In lung cancer research, miRNA signatures have proven useful in detecting early-stage disease and differentiating histological subtypes, suggesting their potential value for early diagnosis and stratification of patients with NSCLC [17,18]. Additionally, serum and

ARTICLE IN PRESS

exosomal miRNAs are often subject to interference and contamination from white blood cells and platelets, making detection of rare circulating tumor miRNAs challenging. In contrast, plasma miRNAs exhibit reduced susceptibility to these interferences [19]. Moreover, traditional assays for miRNA analysis, such as northern blotting, RT-qPCR, microarrays, and next-generation sequencing, are limited by the high cost of instrumentation, narrow detection ranges, extended turnaround times, and the requirement for specialized expertise [20-22]. Consequently, there is a pressing need to develop a biosensing platform that is both efficient and highly precise for plasma miRNAs analysis.

Electrochemical biosensing has become a promising platform for oncological analysis, providing flexible and simple detection in biomedical fields [23]. Recent advancements have expanded these platforms beyond analyte quantification toward clinically actionable outputs, including simultaneous cancer cell characterization and therapeutic evaluation via Kv channel targeting [24], and personalized 5-fluorouracil chemotherapy guidance through direct biosensor-to-clinical decision linkage [25]. However, conventional current- and voltage-based readouts inherently lack the sensitivity required for detecting low-abundance nucleic acid targets like plasma miRNAs, even with dedicated amplification strategies. The electrochemiluminescent (ECL) technique, which uniquely bridges electrochemical excitation and optical signal readout, has been widely applied in biological analysis, mainly due to high sensitivity, excellent controllability, simple operation, and cost effectiveness [26,27]. Compared with conventional amperometric or voltammetric electrochemical methods, ECL uniquely decouples the optical signal readout from the background electrical noise, conferring superior signal-to-noise ratios that are especially beneficial for trace nucleic acid quantification in complex biological matrices like plasma [28]. However, the advancement of the ECL technique is significantly constrained by several challenges associated with the fixation materials for luminous substances, such as low immobilization efficiency, inadequate film-forming properties, and poor biocompatibility, which extremely limit the clinical application of ECL biosensors [29].

ARTICLE IN PRESS

To address these limitations, diverse substrate strategies have been explored. Paper- and cellulose-based ECL platforms exploit the intrinsic porosity of paper substrates for reagent pre-immobilization and have demonstrated promise as low-cost and portable alternatives for point-of-care testing applications [30]. However, the structural and functional constraints of paper substrates render them less amenable to integration with complex signal amplification modules required for low-abundance nucleic acid detection. By contrast, Hydrogel-based ECL platforms offer superior immobilization efficiency and three-dimensional structural versatility. For instance, a self-assembled peptide hydrogel was employed to construct a three-dimensional ECL sensing platform in which luminescent emitters were stably and homogeneously incorporated via noncovalent interactions, enabling sensitive in situ detection of H_2O_2 released from breast cancer cells [31]. Broadly, hydrogel-assisted ECL systems have demonstrated applicability across the detection of hydrogen peroxide, proteins, nucleic acids, and other biomolecules [32]. Building upon these advances, we have incorporated hydrogels into the construction of ECL biosensing platforms, leveraging their large surface area [33], high adhesiveness [34], and good biocompatibility [35]. Importantly, the excellent properties of hydrogels facilitate the seamless integration of ECL biosensing platforms with isothermal nucleic acid amplification modules [36], thereby substantially enhancing overall analytical performance. For instance, self-enhanced luminol-based ECL hydrogels were coupled with a target-initiated DNAzyme motor for ultrasensitive biosensing analysis of fusion genes [29]. Furthermore, a self-enhanced nanohydrogel ECL biosensor based on a CRISPR/Cas12a system was developed for high-sensitivity detection of DNA molecules [37]. Therefore, this robust and efficient strategy ensures high analytical performance while preserving sequence specificity, a critical requirement for detecting rare miRNA targets.

Once the analytical performance of the developed assay has been optimized, a key requirement for differential diagnosis of NSCLC is that the assay output can be rigorously interpreted and translated into clinically actionable indices. Traditional RNA assays, typically dependent on a singular readout for individual target, are susceptible

ARTICLE IN PRESS

to signal fluctuations, exhibit limited accuracy for detecting low-abundance miRNAs, and offer only a partial perspective on the comprehensive transcriptomic changes occurring within the system [38-40]. In contrast, ML algorithms trained on a panel composed of multi-marker miRNA signatures have shown the capability to capture nonlinear dependencies and higher-order interactions, extract stable diagnostic or prognostic signatures, and consistently exceed single-analyte thresholds in terms of robustness and accuracy [41-43]. Therefore, the integration of a high-performance ECL biosensing platform, capable of precisely quantifying miRNA abundance, with an optimally selected ML algorithm offers a rational strategy to enhance NSCLC classification.

Herein, we developed a machine learning-advanced ECL biosensing platform termed hydrogel-based transcription-coupled positive-feedback CRISPR/Cas13a (TCPFC) enhanced ECL analyzer, designed to detect plasma miRNA signatures for differential diagnosis of NSCLC. The developed platform has advantages as follows. First, The Au@ACZ-SA-PEG hydrogels, noted for their easy fabrication, high specific surface area, and superior biocompatibility, present dual benefits of accessibility and exceptional analytical performance, serving as a robust scaffold for the stable co-immobilization of ECL emitters and functional nucleic acid components. Second, the TCPFC strategy employs transcription-coupled positive-feedback CRISPR/Cas13a to achieve cascade signal amplification. Finally, leveraging the precise quantification capabilities described above, the platform enables the identification of novel plasma miRNA signatures for NSCLC and the development of a differential diagnosis model using machine learning, translating multi-miRNA ECL outputs into a robust classifier capable of distinguishing healthy controls from patients across disease stages. To facilitate clinical interpretation, the predicted class probabilities from the optimal classifier were further consolidated into a risk score (RS), a continuous index where higher values indicate an increased likelihood of more advanced NSCLC status. the predicted class probabilities from the optimal classifier were further consolidated into a risk score (RS), a continuous index where higher values indicate an increased

ARTICLE IN PRESS

likelihood of more advanced NSCLC status.

We anticipated that this platform would facilitate an advanced liquid-biopsy strategy and accelerate the clinical translation of multiple miRNA signatures for precision NSCLC management.

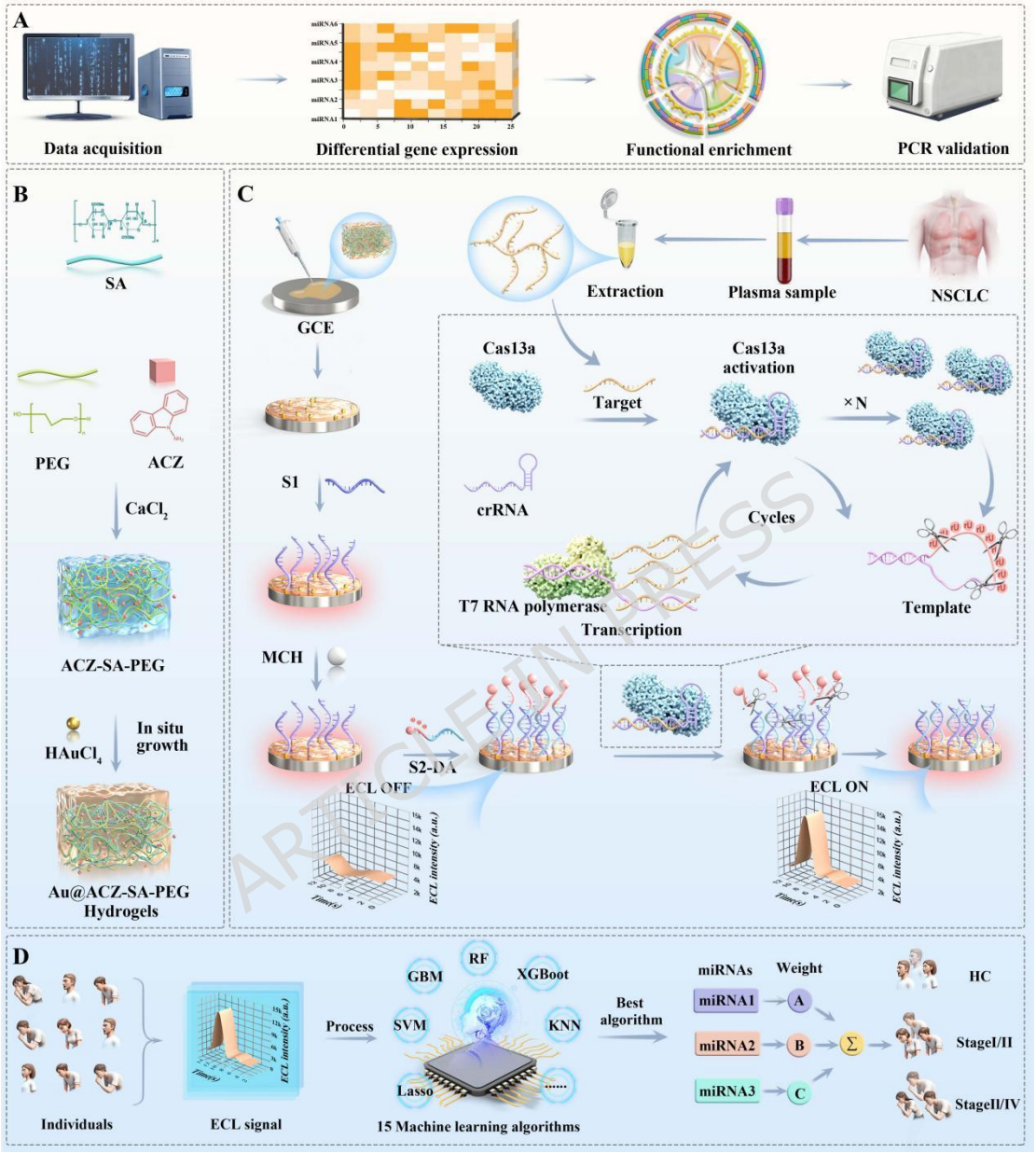
Results and discussion

Principle of the biosensing platform

This study primarily encompasses four pivotal components: (i) Identification and validation of novel miRNA signatures, (ii) The synthesis of Au@ACZ-SA-PEG hydrogels, (iii) The construction of a hydrogel-based TCPFC-enhanced ECL analyzer, and (iv) the construction of a differential diagnosis model using ML algorithms, as illustrated in Scheme 1. For process A, three miRNA signatures (miR-203b, miR-450b, and miR-642a) associated with the initiation and progression of NSCLC were identified by screening plasma miRNA profiles of the healthy controls (HCs) and NSCLC patients in public databases, followed by RT-qPCR validation in independent clinical samples. In process B, the Au@ACZ-SA-PEG hydrogels were synthesized through $CaCl_2$-mediated physical cross-linking of SA, PEG, and ACZ into porous hydrogels, followed by the in situ growth of Au nanoparticles (Au NPs) within the formed matrix. In process C, the Au@ACZ-SA-PEG hydrogels exhibited remarkable ECL response ("ECL ON") on a GCE. The ECL-resonance energy transfer (RET) interface was successfully prepared on the GCE via the immobilization of the thiolated probe (S1), MCH blocking, and hybridization with the dopamine-labeled strand (DA-S2) ("ECL OFF"). Subsequently, targets were incorporated into a unified TCPFC strategy. Upon target recognition, Cas13a was activated, leading to the cleavage of both the template and reporters, while T7 transcription generated abundant triggers with similar targets, creating a positive-feedback loop and cascade signal amplification. Collateral cleavage removed DA from the S1-S2-DA structures, thereby restoring the ECL signal for sensitive sample readout ("ECL OFF"). In process D, ECL responses of the three miRNA signatures were integrated by ML models. In particular, a best algorithm-based score classifier enabled clinical discrimination between HCs and patients with stages

ARTICLE IN PRESS

I/II and III/IV of NSCLC. We anticipated that this approach would enhance precision oncology by integrating biosensing technologies with ML-driven analysis, thereby expediting the differential diagnosis and informing personalized therapeutic monitoring.



Scheme 1. ML-advanced hydrogel-based TCPFC analysis for novel miRNA signatures in differential diagnosis of NSCLC. (A) Identification of three miRNA signatures. (B) The synthesis process of Au@ACZ-SA-PEG hydrogels. (C) Construction of the ECL biosensing platform. (D) Construction of a differential diagnosis model using ML algorithms.

Identification of miRNA signatures

ARTICLE IN PRESS

206 The “limma” package was used to identify differentially expressed miRNAs
207 (DEmiRNAs) between HCs and NSCLC patients. A total of twelve miRNA candidates
208 were screened between the two groups. Five miRNA candidates were significantly
209 downregulated, while seven were upregulated in the NSCLC group compared to the
210 HC group (Figure 1A and B). Then, the seven upregulated miRNA candidates were
211 preliminarily verified by RT-qPCR in an independent cohort (subset 1) of 20 NSCLC
212 patients and 20 HCs. A scatter plot revealed three miRNA candidates (miR-203b, miR-
213 450b, and miR-642a) with a discernible up-regulatory trend in the NSCLC group
214 compared to the HC group (Figure 1C). A receiver operating characteristic (ROC) curve
215 analysis validated the application of the three miRNA candidates in accurately
216 classifying subjects with NSCLC (Figure 1D). This robust validation provided strong
217 evidence for the potential of the three miRNAs as reliable signatures for NSCLC
218 diagnosis. Subsequently, we predicted the target genes of the three miRNA signatures
219 using three bioinformatics databases (TargetScan, miRDB, and miRWalk). A total of
220 two hundred thirteen intersecting genes were identified (Figure 1E). Further analysis of
221 the target genes through KEGG pathway enrichment analysis showed that most target
222 genes were involved in MAPK, cAMP and Wnt signaling pathways, implying that the
223 three miRNA signatures play a crucial role in NSCLC progression (Figure 1F).
224 Therefore, these findings provide preliminary biological plausibility for the candidacy
225 of the three miRNAs as NSCLC-associated diagnostic markers.

ARTICLE IN PRESS

ARTICLE IN PRESS

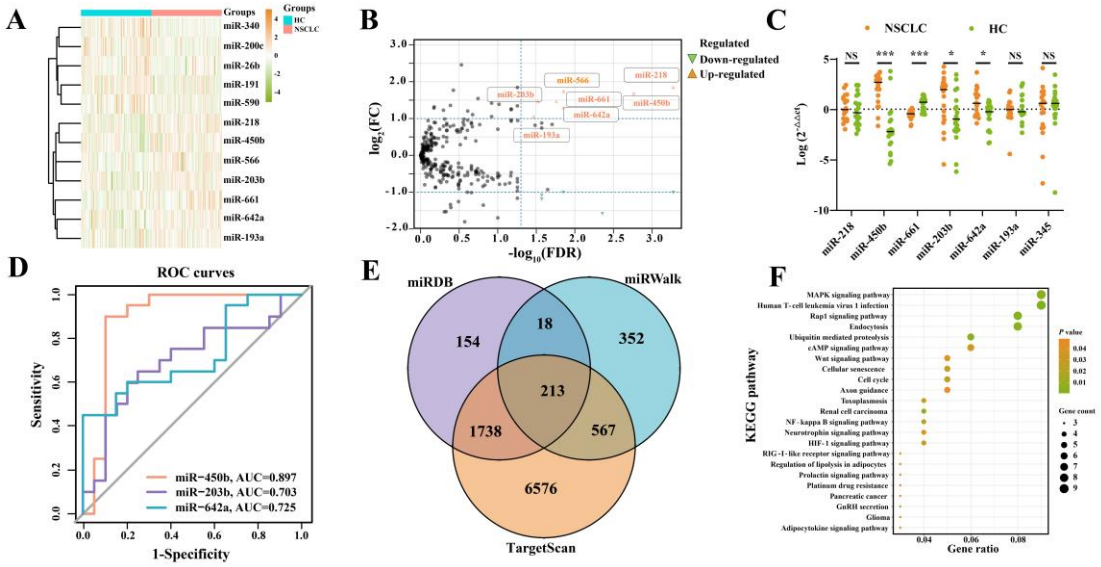


Figure 1. Identification of novel miRNA signatures. (A, B) Heatmap and volcano plots showed DEmiRNAs in plasma between HC and NSCLC groups in the GEO cohort. (C) Validation of upregulated miRNAs by RT-qPCR. (D) ROC curves of diagnosis for NSCLC patients. (E) Venn diagram of target genes of the three miRNA signatures. (F) KEGG enrichment analysis for target genes of the three miRNA signatures. NS: no significance. *p<0.05, ***p < 0.001.

Characterization of Au@ACZ-SA-PEG hydrogels

Atomic force microscopy (AFM) height maps revealed a stepwise evolution of surface topography along the synthetic route (Figure 2A). The Ca^{2+}-crosslinked alginate gel (SA) showed a heterogeneous granular landscape (R_q = 39.2 nm), reflecting the junction-zone heterogeneity inherent to the “egg-box” crosslinking motif [44]. Co-gelation in the presence of PEG (SA-PEG) significantly smoothed the interface (R_q = 8.8 nm). This reduction in roughness was attributed to the formation of a hydrated, conformal PEG coating, known to homogenize surfaces and suppress interfacial irregularities [45]. Subsequent amino-carbazole (ACZ-SA-PEG) partially restored nanoscale texture (R_q = 21.4 nm), a trend consistent with increased roughness commonly observed after additive incorporation in hydrogels/polysaccharide systems [46]. Finally, the in-situ formation of Au NPs on the ACZ-SA-PEG hydrogels resulted in a heterogeneous landscape with abundant protrusions and significant roughening (R_q = 111.0 nm). These results were consistent with previous studies indicating that alginate

ARTICLE IN PRESS

matrices serve as templates for the in-situ nucleation and growth of Au NPs, leading to increased surface relief [47].

Fourier transform infrared spectroscopy (FTIR) spectra confirmed each step of the hydrogel′s synthesis (Figure S1). In the SA-$CaCl_2$ sample (curve a), strong peaks appeared at 1625.3 cm^{-1} and 1416.6 cm^{-1}, corresponding to the asymmetric and symmetric -COO^- stretching vibrations. A broad O-H stretch band at 3438.8 cm^{-1} further indicated intense coordination between Ca^{2+} and carboxylate groups, forming the "egg-box" structure [48]. After adding PEG (curve b), new peaks at 1101.8 and 1146.3 cm^{-1} assigned to C-O-C ether stretches, and a peak at 2883.0 cm^{-1} corresponds to -CH_2- stretches. These features showed that PEG chains were successfully embedded in the network [49,50]. Upon introduction of ACZ (curve c), a characteristic aromatic C=C/C-N stretch appeared at 1503.8 cm^{-1}, and a ring-skeletal resonance peak emerged at 1570.1 cm^{-1} [51]. Besides, A band at 3336.2 cm^{-1} was observed, which is consistent with the N–H stretching vibration of the amino group in ACZ. Finally, in situ growth of Au NPs in the ACZ-SA-PEG hydrogels (curve d) produced a weak peak near 763.1 cm^{-1}, assignable to Au-N coordination [52]. The unchanged positions of the C-O-C and -COO^- peaks indicated that the network framework of hydrogels remained intact during nanoparticle formation.

Scanning electron microscope (SEM) was used to characterize the morphology of as-synthesized porous hydrogels (Figure 2B-D). These results showed that the ACZ-SA-PEG hydrogels were 3D microstructure with multiple pores that could provide a large surface area and a variety of active sites. Further, the elemental distribution of Au@ACZ-SA-PEG hydrogels was verified using energy-dispersive X-ray spectroscopy (EDX) elemental mapping. As depicted in Figure 2E-J, most of the Au NPs were uniformly distributed on the ACZ-SA-PEG hydrogels, and the Au NPs accounted for only a small fraction of the total elemental composition. Subsequently, wide-scan X-ray photoelectron spectroscopy (XPS) survey (Figure 2K) displayed clear signals for C 1s, N 1s, O 1s, and Au 4f, confirming elemental composition and chemical state of Au@ACZ-SA-PEG hydrogels. The high-resolution C1s spectrum could be

ARTICLE IN PRESS

deconvoluted into three distinct carbon species (Figure S2A): a dominant peak at ~284.8 eV (C-C/C-H), and a higher-energy shoulder around ~287.2 eV attributable to C=O, in excellent agreement with previously reported assignments [53]. In the N 1s region, peaks at ~399.9 eV (pyridinic N) and ~401.7 eV (graphitic N) were observed (Figure S2B), while O 1s spectra revealed contributions from lattice oxygen (~532.1 eV) and adsorbed oxygen species (~535.9 eV) (Figure S2C). The Au 4f region displayed a characteristic doublet with binding energies around 83.7 eV (Au^0, $4f_{7/2}$) and 87.6 eV (Au^{3+}, $4f_{5/2}$), indicating that the gold is predominantly present in the zerovalent state at the composite interface (Figure S2D) [54]. As presented in Figure 2L, the XRD profile of the ACZ-SA-PEG hydrogels exhibited two broad, diffuse halos at 2θ values of 16.7° and 20.3°. These features were characteristic of a predominantly amorphous structure with limited short-range ordering within the polymer network [55]. Notably, a sharp bragg reflection appeared at ~38.1°, corresponding to the plane of metallic Au. This crystalline feature confirmed the successful in situ reduction and homogeneous dispersion of Au NPs within the ACZ-SA-PEG hydrogels. The N_2 adsorption-desorption isotherm of ACZ-SA-PEG hydrogels exhibited a typical type-IV profile, with a gradual uptake at low relative pressure and a steep rise as P/P_0, consistent with capillary condensation in a porous network. As shown in Figure 2M, ACZ-SA-PEG hydrogels showed a BET surface area of 9.75 $m^2\ g^{-1}$ and a total pore volume of 0.032 $cm^3\ g^{-1}$, with an average pore diameter of 5-6 nm, confirming abundant accessible mesopores. In contrast, Au@ACZ-SA-PEG hydrogels displayed a much lower N_2 uptake over the entire pressure range, giving a reduced BET area of 6.31 $m^2\ g^{-1}$ and a smaller pore volume of 0.014 $cm^3\ g^{-1}$, with an average pore diameter of 3-4 nm. The simultaneous decreases in surface area and pore volume indicated that introducing Au NPs partially filled or constricted the intrinsic mesopores, thereby reducing the number of accessible adsorption sites rather than creating new porosity [56]. Consistently, BJH analysis of the desorption branch showed mesopore-centred distributions for both materials with the main feature remaining in the 2-5 nm regime, supporting the view that Au loading chiefly blocks channels while preserving the mesoporous framework

ARTICLE IN PRESS

(Figure S3) [57]. Therefore, these results indicated that Au@ACZ-SA-PEG hydrogels were synthesized successfully.

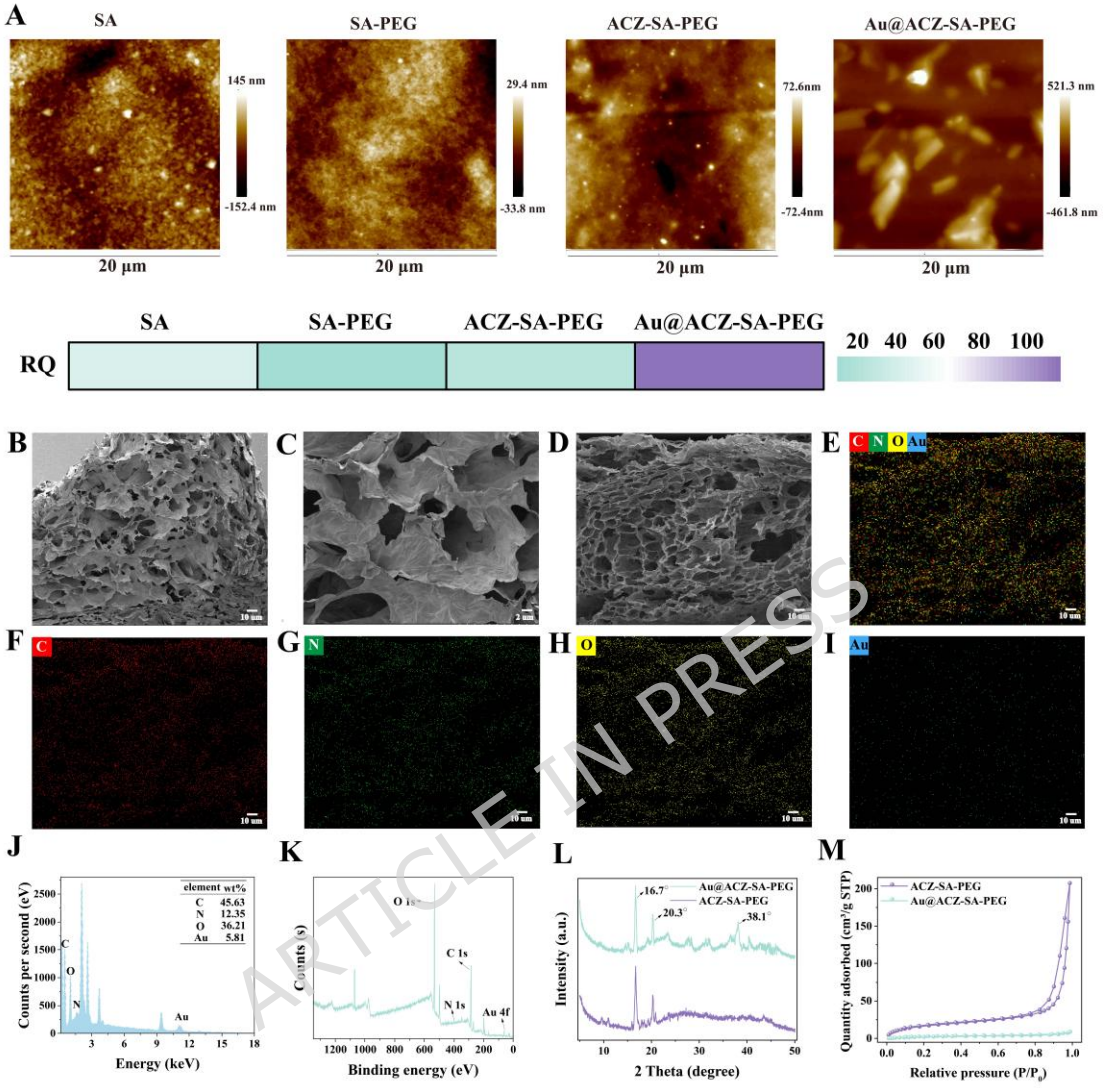


Figure 2. Characterization of Au@ACZ-SA-PEG hydrogels. (A) AFM for the synthetic characterization of SA, SA-PEG, ACZ-SA-PEG, and Au@ACZ-SA-PEG hydrogels. Scale bar, 20 μm. (B-D) SEM images of Au@ACZ-SA-PEG hydrogels. (E-J) Corresponding EDX element mapping images of C, N, O, Au, and merge. (K) XPS analysis for the full region of Au@ACZ-SA-PEG hydrogels. (L) XRD pattern of ACZ-SA-PEG and Au@ACZ-SA-PEG hydrogels. (M) N_2 adsorption-desorption curve of ACZ-SA-PEG and Au@ACZ-SA-PEG hydrogels.

Feasibility validation of the TCPFC strategy

The reaction process of the TCPFC strategy was illustrated in Figure 3A. Specifically,

ARTICLE IN PRESS

the CRISPR/Cas13a assay utilized a strategically designed crRNA to recognize the target and form a Cas13a-crRNA complex. In the absence of the target, Cas13a remained inactive. However, upon target recognition, the complex underwent conformational activation, initiating intensive non-specific degradation of the RNA templates and FAM-BHQ-labeled ssRNA reporters. This degradation led to the separation of the fluorophore from the quencher, resulting in a significant fluorescence signal. Simultaneously, T7 RNA polymerase (T7 RNAP) was employed to generate abundant triggers with similar targets, resulting in cascade signal amplification. In order to validate the feasibility of the TCPFC strategy, we first conducted 12% PAGE analysis. As shown in Figure 3B, lane 5 displayed four nucleic-acid bands with distinct electrophoretic mobilities, indicating that in the absence of Cas13a, the RNA segments within the template substrate were not sheared. In lane 6, the observation of discrete fragments derived from the template strand confirmed that the formation of the crRNA-target duplex activated Cas13a, which subsequently mediated the cleavage of the template strand. Significantly, Lane 7 revealed the simultaneous presence of Cas13a-cleaved fragments and abundant T7 RNAP-generated transcripts. These results demonstrated that the crRNA-target duplex not only triggered Cas13a-mediated cleavage but also fueled T7 RNAP-driven transcription to yield a large quantity of similar target RNAs. Likewise, fluorescence kinetic analysis confirmed the activity of the TCPFC strategy (Figure 3C), demonstrating that the inclusion of both Cas13a/crRNA and T7 RNA polymerase increased the fluorescence intensity compared to Cas13a/crRNA alone (curves f and g). Subsequently, we investigated the linear detection range and limit of detection (LOD) of the TCPFC strategy for the three miRNA signatures by fluorescence spectroscopy. The results revealed that fluorescence signals increased continuously with the rising target concentration. The detection ranges of the Logic-Measurer were 10 fM to 10 nM (Figure 3D-F). The fluorescence intensity exhibited linearity with the target concentration (lg$C$) over the examined range, with the following calibrations: I = 613.2 lg$C_{(\text{miR-203b})}$ + 362.1 (R = 0.994), I = 648.2 lg$C_{(\text{miR-450b})}$ + 155.2 (R = 0.988), and I = 759.9 lg$C_{(\text{miR-642a})}$ + 64.9 (R = 0.991) (Figure

ARTICLE IN PRESS

346 3G-I), with a LOD of 8.12 fM, 4.95 fM, and 8.86 fM, respectively (Figure S4). In
347 comparison, Cas13a-based detection without amplification has been reported to achieve
348 a LOD of approximately 38 pM [58], representing a 4,200 to 7,600-fold improvement
349 in sensitivity attributable to the TCPFC positive-feedback amplification. Collectively,
350 these results indicated that the TCPFC strategy employed the transcription-coupled
351 positive-feedback CRISPR/Cas13a to achieve cascade signal amplification.

ARTICLE IN PRESS

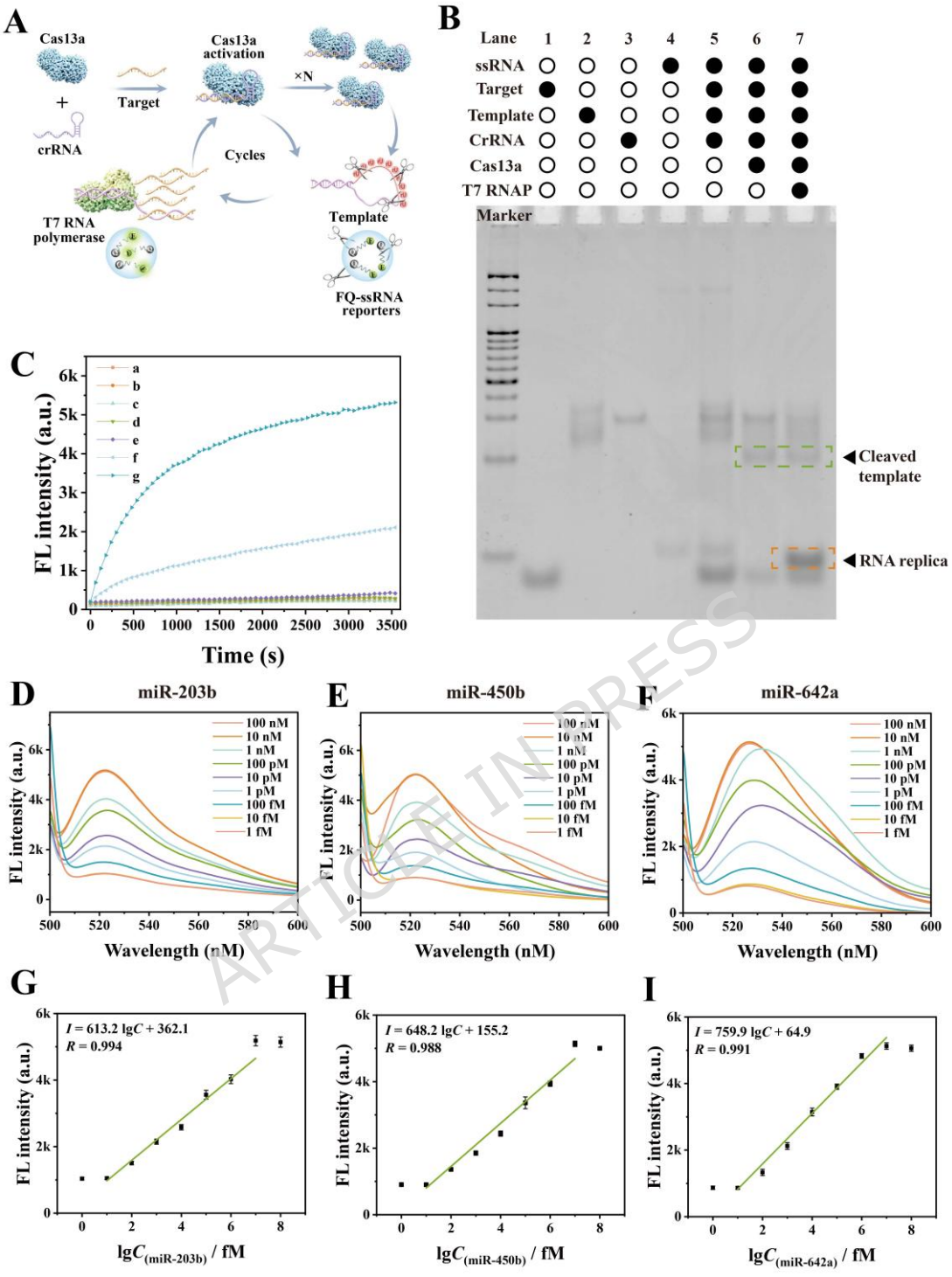


Figure 3. Feasibility validation of the TCPFC strategy. (A) Schematic diagram of the TCPFC strategy. (B) PAGE images of the TCPFC strategy. (C) Fluorescence kinetic analysis of the TCPFC strategy (a: Target, b: Template, c: Cas13a-CrRNA, d: Reporters, e: ssRNA+Template+Cas13-CrRNA+T7 RNA polymerase, f: ssRNA + Target + Template + Cas13a-CrRNA, and g: ssRNA + Target + Template + Cas13-CrRNA + T7

ARTICLE IN PRESS

RNA polymerase). (D-F) The fluorescence intensity from the addition of different concentrations from 1 fM to 100 nM of the three miRNA signatures based on the TCPFC strategy. (G-I) Linear analysis of the three miRNA signatures by the TCPFC strategy.

Characterization of the ECL biosensing fabrication

In order to explore the ECL properties of Au@ACZ-SA-PEG hydrogels, the ECL characteristics of Au@ACZ-SA-PEG hydrogels were examined in an aqueous solution. Based on established methodologies demonstrating that co-reactants such as triethylamine (TAE), tripropylamine (TPE), hydrogen peroxide (H_2O_2), and potassium persulfate ($K_2S_2O_8$) can enhance the ECL performance of luminophores, we conducted a comprehensive screening to evaluate the impact of various potential co-reactants. Notably, only the presence of $K_2S_2O_8$ resulted in a significant increase in the ECL signal of Au@ACZ-SA-PEG hydrogels (Figure S5A, B). The possible working principle underlying ECL analytical performance in the assembled device was illustrated in the schematic of Figure S5C. Under cathodic polarization, the ACZ entrapped within the Au@ACZ-SA-PEG hydrogels underwent electrochemical reduction to generate $ACZ^{\bullet-}$. Simultaneously, the co-reactant $S_2O_8^{2-}$ was reduced at the electrode surface, yielding sulfate radical anions ($SO_4^{\bullet-}$) and sulfate ions (SO_4^{2-}). The presence of Au NPs significantly accelerated interfacial electron transfer, thereby enhancing the yield of $SO_4^{\bullet-}$. Subsequently, the highly reactive $SO_4^{\bullet-}$ interacted with $ACZ^{\bullet-}$ to generate the excited-state ACZ*, whose radiative decay resulted in the emission of a photon ($h\nu$), resulting in the ECL emission. Upon the introduction of DA, its electrochemically oxidized form functioned as an energy acceptor, engaging with the excited ACZ* via an electrochemically induced resonance energy transfer (RET) process. This led to the non-radiative dissipation of excitation energy, effectively quenching the ECL output. This classic RET-based quenching mechanism relied on the spectral overlap between ACZ emission and DA absorption and occurred efficiently due to the nanoscale proximity of DA to ACZ, consistent with effective RET behavior in nanomaterial-based ECL systems [59]. To directly substantiate the enhancement in electron transfer and

ARTICLE IN PRESS

radical generation efficiency, comparative ECL intensities and electrochemical kinetic parameters were measured for SA-PEG, ACZ-SA-PEG, and Au@ACZ-SA-PEG under identical conditions. As shown in Figure S6A, the ECL intensity followed the order Au@ACZ-SA-PEG > ACZ-SA-PEG > SA-PEG, with Au@ACZ-SA-PEG yielding the highest ECL signal (~17,000 a.u.), confirming the progressive enhancement afforded by ACZ incorporation and subsequent Au NPs. Cyclic voltammetry (CV) (Figure S6B) further revealed that Au@ACZ-SA-PEG exhibited larger redox peak currents and a smaller peak-to-peak potential separation (ΔEp) compared to ACZ-SA-PEG, indicating superior electron transfer kinetics. Consistently, electrochemical impedance spectroscopy (EIS) plots (Figure S6C) demonstrated that Au@ACZ-SA-PEG possessed a significantly smaller charge electron-transfer resistance (R_{et}) than ACZ-SA-PEG, providing direct impedimetric evidence for accelerated interfacial electron transfer.

Reaction sequence:

1.ACZ + e^- → $ACZ^{\bullet-}$

2.$S_2O_8^{2-}$ + e^- → $SO_4^{\bullet-}$ + SO_4^{2-}

3.Au-mediated: $S_2O_8^{2-}$ + e^- → $SO_4^{\bullet-}$ (enhanced yield) + SO_4^{2-}

4.$ACZ^{\bullet-}$ + $SO_4^{\bullet-}$ → ACZ* + SO_4^{2-}

5.ACZ* → ACZ + *hv* (ECL emission)

6.ACZ* + DA-oxidation product → non-radiative RET → ECL quenching

To confirm the stepwise modification of the ECL biosensing interface, EIS and CV measurements were conducted in 5.0 mM $[Fe(CN)_6]^{3-/4-}$ solution containing 0.1 M KCl. As illustrated in Figure S7A, the bare electrode displayed a small semicircle (curve a), indicative of the low electron-transfer resistance (R_{et}) associated with $[Fe(CN)_6]^{3-/4-}$. When the Au@ACZ-SA-PEG hydrogels were applied to the electrode, the R_{et} value increased (curve b), which could be attributed to the obstruction of electron transfer caused by the hydrogel layer. Subsequent sequential modifications, including the immobilization of the S1 probes (curve c), blocking of unbound sites with MCH (curve d), and attachment of DA-S2 (curve e), resulted in a progressive increase at R_{et} due to the poor conductivity of both the oligonucleotide strands and MCH. Upon incubation

ARTICLE IN PRESS

with the TCPFC strategy, Cas13a-mediated cleavage of S1-S2-DA resulted in the removal of the DA moiety from the biosensing interface, thereby reducing the R_{et} (curve f). Furthermore, CV profiles mirrored the changes observed in the EIS measurements (Figure S7B), offering consistent electrochemical evidence for the successful assembly of the device. Subsequently, the feasibility of the biosensing strategy was evaluated by integrating the TCPFC strategy on the GCE surface. As shown in Figure S8A, when the Au@ACZ-SA-PEG hydrogels were incubated on the GCE surface, a strong ECL signal was observed (curve a). Upon subsequent immobilization of the S1-S2-DA structure onto the GCE electrode, the ECL intensity was markedly quenched (curve b). Introduction of the target′s analyte followed by activation of the TCPFC strategy restored the ECL emission to its original level (curve c). The reversible "ON-OFF-ON" transitions facilitated seamless integration of the ECL biosensing platform with the TCPFC strategy, achieving high analytical performance.

To maximize analytical performance of the fabricated ECL biosensor, key experimental parameters of the ECL biosensor were systematically optimized. Firstly, the TCPFC strategy was a key factor influencing analytical performance of ECL detection. The primary variables influencing this strategy included the concentrations of the Cas13a/crRNA complex, T7 RNA polymerase, and the template strand, as well as the reaction time. As illustrated in Figures S8B-D, the ECL intensity increased as the concentration of each component was raised within a specific range. When the concentrations of the Cas13a/crRNA complex, T7 RNA polymerase, and the template strand reached 80 nM, 80 nM, and 320 nM, respectively, the ECL signal no longer showed a noticeable increase. Therefore, these values were selected as the optimal concentrations for each component. Figure S8E demonstrated that the ECL signal reached its peak after 30 minutes of reaction time, followed by a slight decline when the reaction extended beyond this duration. Consequently, a 30 minutes incubation was determined to be the optimal reaction time. Additionally, the quenching effect of DA was crucial for resetting the ECL signal prior to target detection, and its concentration significantly influenced the quenching efficiency. Figure S8F showed that among

ARTICLE IN PRESS

various DA concentrations tested on the electrode, 40 nM DA resulted in the greatest restoration of the ECL signal. When the DA concentration exceeded 40 nM, the signal recovery efficiency decreased with increasing concentration. Therefore, 40 nM was selected as the optimal quencher concentration.

Analytical performance of the fabricated ECL biosensor

In optimal experimental conditions, the analytical performance of the fabricated biosensor for three miRNA signatures (miR-203b, miR-450b, miR-642a) was validated. Figure 4A-C presented ECL intensity-time curves of the ECL biosensor in response to increasing concentrations of three miRNA signatures, exhibiting a progressive increase in signal with rising analyte levels. As shown in Figure 4D-F, a strong linear relationship was observed between the logarithm of the miRNA concentration (ranging from 100 aM to 1 nM) and ECL intensity, described by the regression equation I = 1785.8 log $C_{(\text{miR-203b})}$ – 1941.2 (R = 0.991), I = 1723.08 log $C_{(\text{miR-450b})}$ -1699.48 (R = 0.989), and I = 1725.96 log $C_{(\text{miR-642a})}$ – 1671.67 (R = 0.987), with a LOD of 68.82 aM, 86.67 aM, and 63.61 aM, respectively (Figure S9). Comparative analysis presented in Table S5 illustrated that the fabricated ECL biosensor outperformed many reported methods by combining a notably low detection limit and broad linear range, offering a more sensitive platform for miRNAs assay.

The specificity of the fabricated ECL biosensor was evaluated, which is essential for implementing accurate analysis of the three miRNA signatures. As shown in Figure 4G-I, potential interferents at 10 pM, which was ten times the concentration of the target miRNA at 1 pM, produced an ECL signal indistinguishable from the blank. In contrast, the target miRNA alone and mixture containing both the target and interferents generated significantly stronger ECL signals than the blank. Together, these results indicated that the ECL biosensor exhibited a specific analysis to the three miRNA signatures. Meanwhile, stability was another crucial characteristic to consider in the ECL biosensor design. The ECL stable performance of the biosensor was explored at 100 aM, 10 fM, 10 pM and 10 nM under 3 cycles of potential scanning as shown in Figure S10A. The calculated relative standard deviation (RSD) was 1.05 %, 1.01 %,

ARTICLE IN PRESS

1.13 % and 3.06 %, respectively, indicating the excellent stability of the fabricated ECL biosensor. Similarly, the intra- and inter-assay repeatability of the ECL platform was evaluated using six parallel replicates (Figure S10B and S10C). The RSDs were 2.73% and 2.48%, respectively, indicating acceptable precision. A batch of biosensors was stored at 4 ° C and its stable performance was evaluated at various time intervals. As shown in Figure S10D, there was no significant change in the ECL signal even after 20 days (RSD = 1.91%), indicating satisfactory storage stability. Then, the average recovery and RSD were further calculated by the relevant formula. The range of the recovery rate was 102.49%-107.11%, whereas the range of the RSD was 0.98%-2.14% (Table S6). Using the ECL biosensor, the three miRNA signatures were detected from the collected samples (subset 1). To further verify the analytical performance, co-expression analysis was conducted between the expression levels of the three miRNA signatures in clinical samples measured by the reference RT-qPCR method and the ECL biosensor (subset 1). As shown in Figure 4J-L, measurements from the two approaches were measurably correlated across the three miRNA signatures, supporting the reliability of the ECL biosensor. Meanwhile, the ECL platform completed each assay within 33.34 min at a per-reaction reagent cost of $5.75 (Table S7), offering a 54-min reduction in turnaround time relative to RT-qPCR (87.64 min; $5.92) at a slightly lower cost, indicating favorable practical applicability. Therefore, these results indicated that the fabricated ECL biosensor possessed satisfactory analytical performance for miRNAs assay.

ARTICLE IN PRESS

ARTICLE IN PRESS

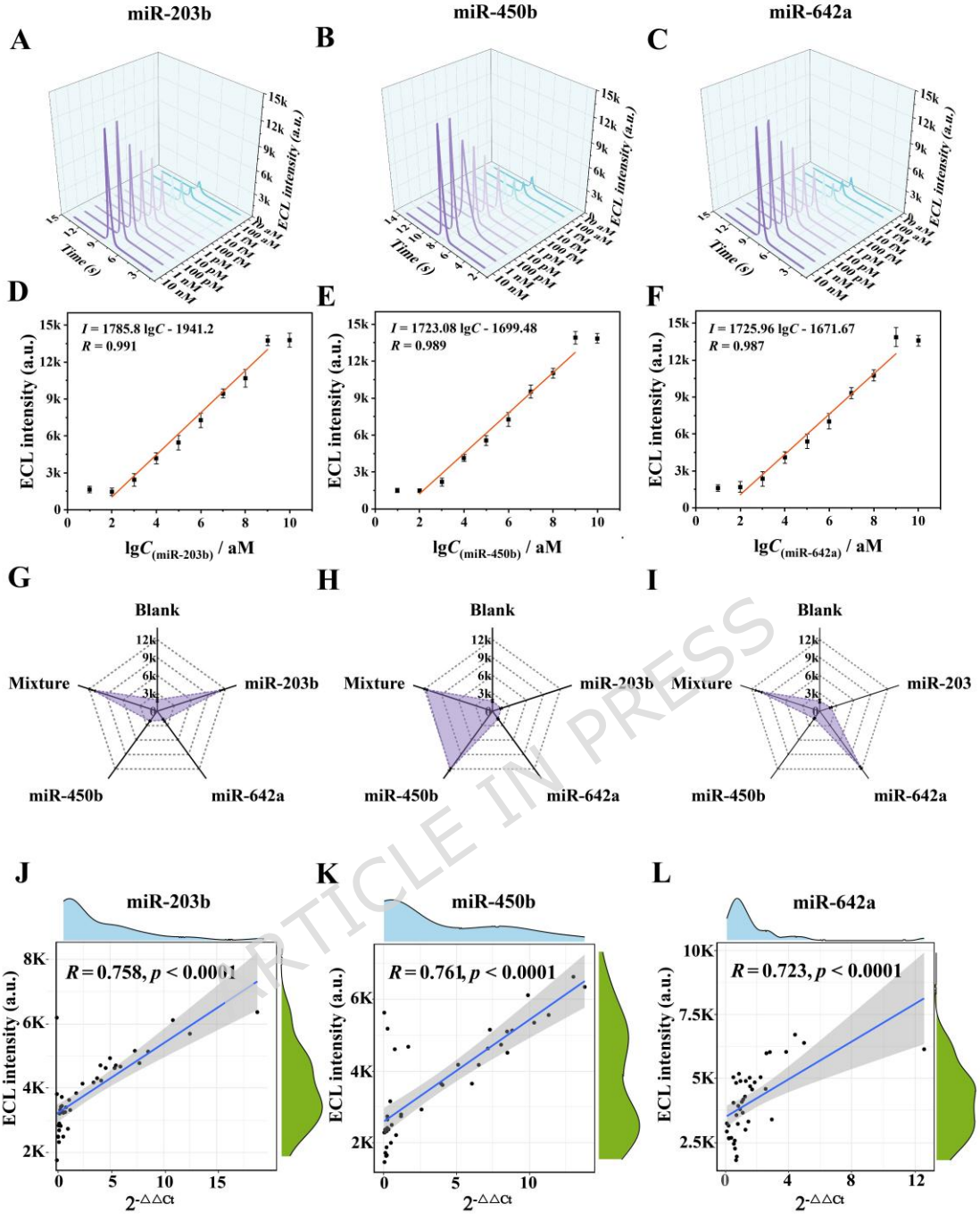


Figure 4. Analytical performance of the fabricated ECL biosensor. (A-C) ECL intensity-time curves to different concentration of three miRNAs (10 aM to 10 nM). (B-F) Calibration plot of the ECL biosensor for the three miRNAs detection. (G-I) Specificity of the ECL biosensor for the miRNA signatures. (J-L) Correlation between the parallel detection (n = 20) by the constructed ECL biosensor and RT-qPCR.

ARTICLE IN PRESS

Human plasma sample test

To preliminarily evaluate the potential clinical application of the fabricated ECL biosensor in the diagnosis of NSCLC, we quantify the three miRNA signatures in plasma specimens from 140 NSCLC patients (Stage I/II, n = 40; Stage III/IV, n = 100) and 80 HCs (subset 2). As shown in Figure 5A, B, the three miRNA signatures displayed a stepwise increase across the HC, stage I/II, and stage III/IV groups. Principal component analysis (PCA) was used to assess the discriminatory power of the three miRNA signatures across groups. These results demonstrated effective separation of samples from the three groups, although a minor degree of overlap persisted (Figure 5C). In addition, ROC analysis was used to evaluate the clinical diagnostic performance of the candidate biomarkers. The results showed that the three miRNA signatures (AUC: 0.857-0.998) exhibited excellent discriminative diagnostic ability (Figure 5D-F). In addition, we classified the same samples using clinically routine lung cancer biomarkers, including CEA, SCCA, and CYFRA21-1. The AUC values for these biomarkers were 0.461-0.727, evidencing inferior accuracy relative to the fabricated approach (Figure 5G-I).

ARTICLE IN PRESS

ARTICLE IN PRESS

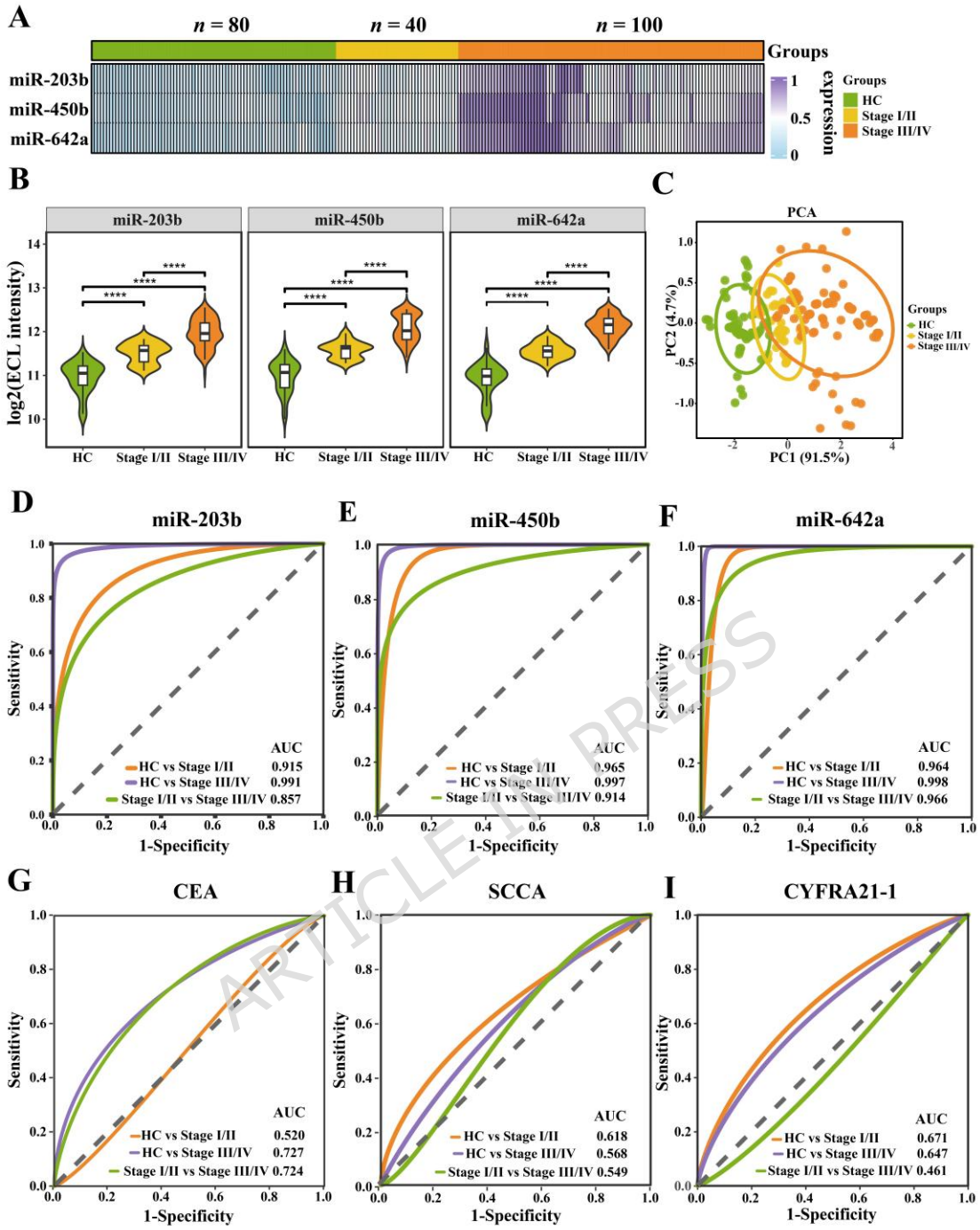


Figure 5. (A) Heatmap of the three miRNA signatures from 220 human samples (HC, $n = 80$; stage I/II, $n = 40$, and stage III/IV, $n = 100$). (B) Distribution violin plots of the three miRNA signatures among the HC, stage I/II, and stage III/IV groups. (C) Plot of the PCA of the three miRNA signatures. (D-I) ROC curves of the three miRNA signatures, CEA, SCCA and CYFRA21-1 in the diagnosis of HC, stage I/II, and stage III/IV groups. ****$p < 0.0001$.

ARTICLE IN PRESS

Clinical differential diagnosis of NSCLC coupled with machine learning

Although these three miRNA signatures were individually capable of robustly discriminating between NSCLC patients and HCs, enhancing their discriminative power among HCs, stage I/II, and stage III/IV groups was essential for clinical prognosis and personalized treatment. Hence, a total of 16 ML algorithms were integrated into a 5-fold cross-validation process to identify the most robust diagnostic model based on the three miRNA signatures for the train and test cohorts. As shown in Figure 6A, the GBM model performed with the highest average AUC value (1.000) in distinguishing HCs, stage I/II, and stage III/IV groups across the train cohort. To formally exclude overfitting, two complementary permutation tests (Y-scrambling, n = 1,000 each) and learning curves were performed on the optimal GMB model, confirming that the high diagnostic performance reflects genuine biological signal rather than modeling artifacts (Figure S11 and S12). Thereby, the GBM model was identified as an optimal model, and the importance of each miRNA as a predictor variable was evaluated in the model. MiR-642a provided the heaviest weight model amongst the 3 predictors (Figure 6B). Based on algorithm of GBM model, we computed RS based on a panel of the three miRNA signatures for each sample. As shown in Figure 6C, there were statistically significant differences in RS among HCs, stage I/II, and stage III/IV groups in the train cohort. Furthermore, the RS exhibited no sample overlap, indicating superior discrimination among groups compared to the three miRNA signatures measurements prior to model construction in the train cohort (Figure 6D). To facilitate the evaluation and explanation of the RS performance in identifying the samples, several confusion matrices were separately constructed based on RS, CEA, SCCA, and CYFRA21-1. Leveraging the RS, discrimination among HCs, stage I/II, and stage III/IV groups achieved an overall accuracy of 100.00%, a precision of 100.00%, a specificity of 100.00%, and a sensitivity of 100.00%, substantially exceeding those obtained with CEA (an overall accuracy of 40.00%, a precision of 57.41%, a specificity of 66.83%, and a sensitivity of 39.00%), SCCA (an overall accuracy of 38.18%, a precision of 38.75%, a specificity of 67.91%, and a sensitivity

ARTICLE IN PRESS

of 41.83%), and CYFRA21-1(an overall accuracy of 58.81%, a precision of 56.02%, a specificity of 76.96%, and a sensitivity of 50.00%) in the train cohort (Figure 6E-H). Meanwhile, the classification results from the ROC curves further confirmed that the RS demonstrated superior diagnostic efficacy (AUC: 1.000, Figure 6I) for the differential diagnosis of HCs, stage I/II, and stage III/IV groups compared with those of the CEA, SCCA, and CYFRA21-1 (AUC: 0.366-0.759, Figure 6J-L). To evaluate the diagnostic relevance of clinical variables, both univariate and multivariate logistic regression analyses were constructed in the train set. Among all factors examined, RS emerged as the sole independent predictor, demonstrating superior discriminatory ability compared to each of the clinical parameters assessed (Figure S13). Given the excellent diagnostic potential demonstrated by the RS in the train cohort, we further assessed its diagnostic accuracy in the test cohort. The analysis results of the RS boxplot reaffirmed its significant heterogeneity potential in distinguishing HCs from NSCLC (Figure 7A). PCA plot also showed a clear demarcation among the HCs, stage I/II, and stage III/IV groups (Figure 7B). Following the same cut-off value from the train cohort, confusion matrix of RS demonstrated an overall accuracy of 92.73%, a precision of 91.68%, a specificity of 96.08%, and a sensitivity of 88.67%, which still substantially outperformed commonly used plasma markers in clinical practice (Figure 7C-F). Consistent with expectations, ROC analysis of the validation cohort showed that the RS achieved the optimal diagnostic performance for discriminating HCs vs stage I/II of NSCLC (AUC = 0.995), HCs vs stage I/II of NSCLC (AUC = 1.000), and stage I/II vs stage III/IV of NSCLC (AUC = 0.911) (Figure 7G-J). As expected, RS was also the only independent predictor across all three comparisons in both univariable and multivariable logistic regression (Figure S14). Therefore, these results provided compelling evidence that the differential diagnosis model constructed using ML algorithms enabled accurate diagnosis and staging of NSCLC.

ARTICLE IN PRESS

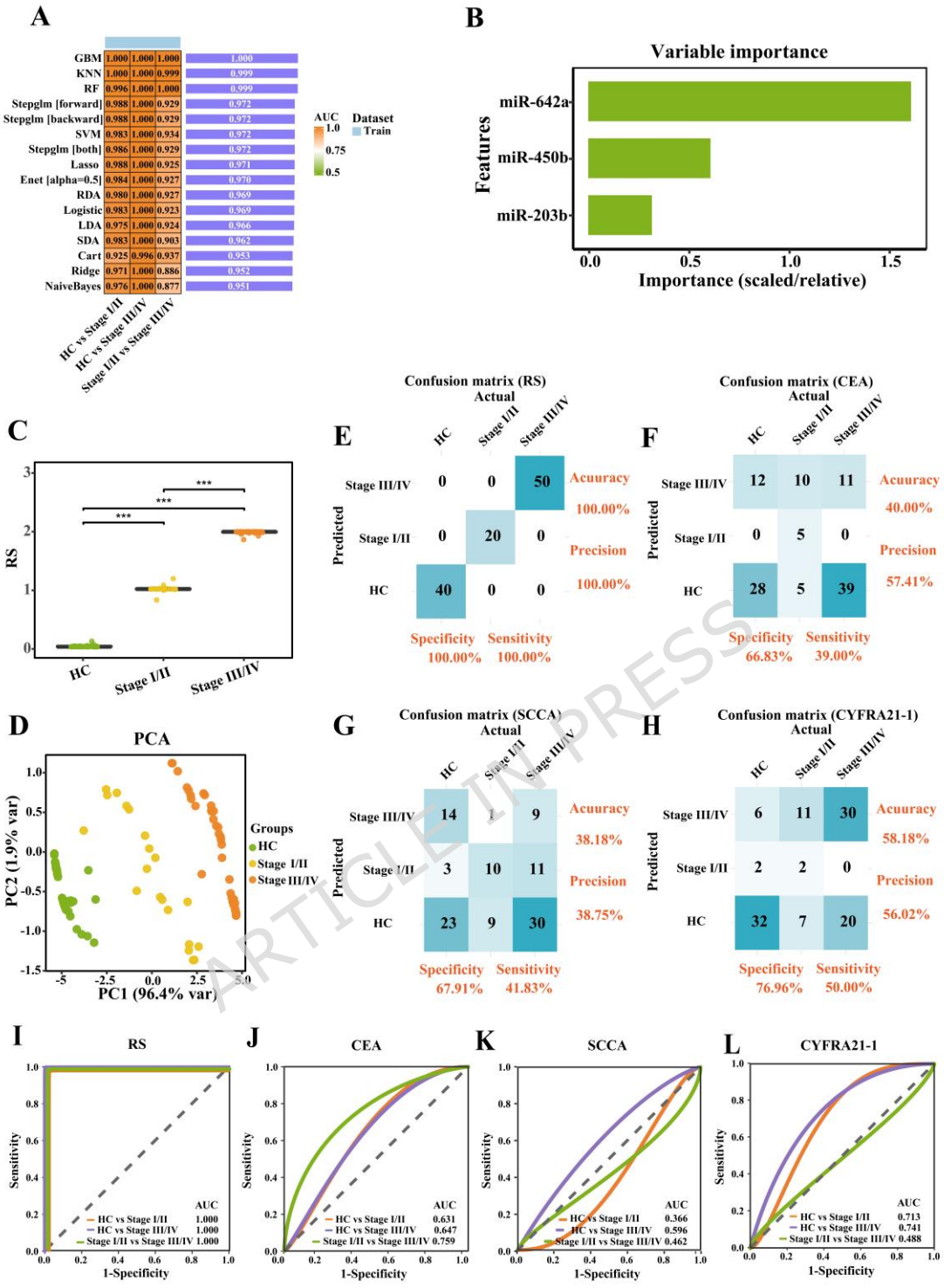


Figure 6. The fabricated ECL biosensor for the differentiation of the HCs, stage I/II, and stage III/IV groups in the train cohort. (A) The AUC of 16 kinds of diagnostic models constructed by 16 learning algorithms in train and test cohort. (B) Variable importance ranking diagram of the GBM model in train cohort. (C) Scatter plots of the RS between the HCs, stage I/II, and stage III/IV groups in train cohort. (D) Plot of the

ARTICLE IN PRESS

PCA of RS in train cohort. (E-H) Confusion matrixes of recognition results for the three groups based on the RS, CEA, SCCA, and CYFRA21-1 in train cohort. (I-L) ROC curves of RS, CEA, SCCA, and CYFRA21-1 in the diagnosis of the HC, stage I/II, and stage III/IV groups in train cohort. ***$p < 0.001$.

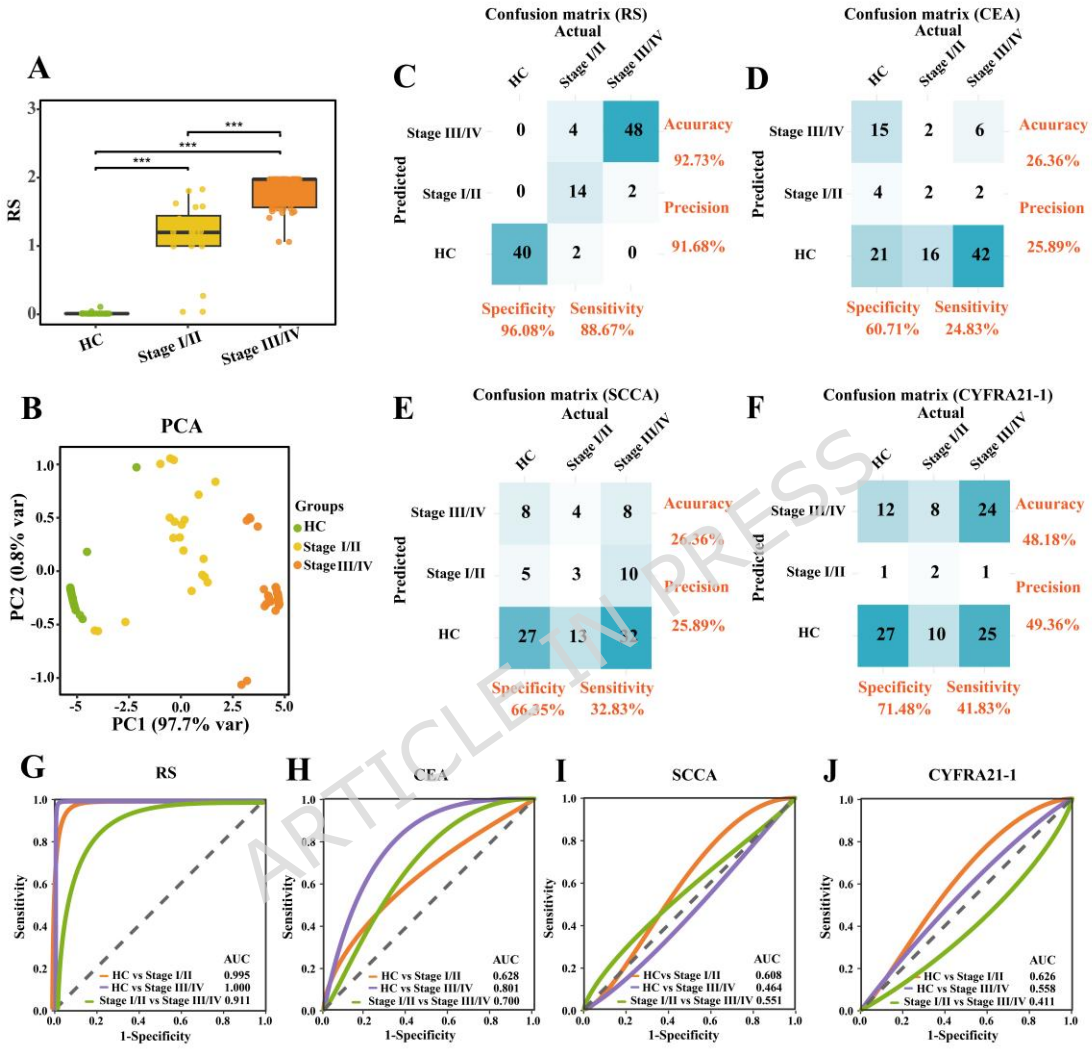


Figure 7. The fabricated ECL biosensor for the differentiation of the HC, stage I/II, and stage III/IV groups in the test cohort. (A) Scatter plots of the RS between the HC, stage I/II, and stage III/IV groups in test cohort. (B) Plot of the PCA of RS in test cohort. (C-F) Confusion matrixes of recognition results for the three groups based on the RS, CEA, SCCA, and CYFRA21-1 in test cohort. (G-J) ROC curves of RS, CEA, SCCA, and CYFRA21-1 in the diagnosis of the HC, stage I/II, and stage III/IV groups in test cohort. ***$p < 0.001$.

Conclusions

ARTICLE IN PRESS

In summary, we have developed a ML-advanced hydrogel-based TCPFC analysis for novel miRNA signatures, prioritized from public plasma miRNA datasets and validated by RT-qPCR. The TCPFC strategy employed transcription-coupled positive-feedback CRISPR/Cas13a to achieve cascade signal amplification, resulting in an approximately femtomolar-level detection limit. Furthermore, the conductive 3D scaffold, along with the large surface area, high adhesiveness, and superior biocompatibility of Au@ACZ-SA-PEG hydrogels, facilitated the innovative development of an ECL biosensing platform utilizing the TCPFC strategy. This led to a significant enhancement in analytical performance, achieving a LOD that was 78-fold lower than that of the conventional TCPFC strategy. Additionally, the integration of distinct RS distributions with the ML-advanced ECL platform resulted in differential diagnostic accuracies of 97.27% for the train cohort (n = 110) and 93.64% for the validation cohort (n = 110), effectively distinguishing between HCs and patients with stages I/II and III/IV of NSCLC. This data-driven approach not only improved diagnostic accuracy but also revealed ML algorithms applicable across the differential diagnosis, highlighting its potential for clinical prognosis. Nevertheless, the current study was performed within a single-center cohort, and the sample size remains limited. To ensure the generalizability of the identified miRNA signatures and the robustness of the diagnostic model, external validation across multicenter cohorts with larger and more diverse patient populations will be crucial before considering broader clinical implementation.

Experimental section

Materials and reagents

Materials, Reagents, Apparatus, total RNA extraction, and RT-qPCR assay steps were listed in the Supporting Information.

Identification of differentially expressed miRNAs in plasma

GSE64591 was downloaded from gene expression omnibus (GEO) database (https://www.ncbi.nlm.nih.gov/geo/), which included 100 plasma samples from NSCLC patients and 100 plasma samples from HCs. The data were sequenced based on GPL18942. Differentially expressed miRNAs (DEmiRNAs) in NSCLC were

ARTICLE IN PRESS

screened using "limma" in R package [60]. False discovery rate (FDR) < 0.05 and |$\log_2$ fold change (FC)| >1 were defined as thresholds for screening DEmiRNAs. Pathway enrichment analyses of genes using the Kyoto Encyclopedia of Genes and Genomes (KEGG) were conducted through the Database for Annotation, Visualization, and Integrated Discovery (DAVID) (https://davidbioinformatics.nih.gov/summary.jsp). *P* value < 0.05 was used as the cut-off criterion for KEGG pathway enrichment analyses.

Synthesis of Au@ACZ-SA-PEG hydrogels

Firstly, ACZ-SA-PEG hydrogels were synthesized by physical cross-linking [61]. In 4 mL of 2% SA and 0.04% PEG aqueous, 100 μL of 40 mM ACZ solution and 250 μL of 0.1 M $CaCl_2$ were successively added, and stirred the mixture at 500 rpm at room temperature (RT) for 1 hour, and then allowed to stand undisturbed for 5 hours. After these hydrogels have fully formed, they should be thoroughly washed three times with deionized water to remove any ungelled components. Subsequently, gold nanoparticles (Au NPs) were synthesized on the surface of the hydrogels, which was achieved by adding 288 μL of $HAuCl_4 \cdot 6H_2O$ (1.0 wt%) to the synthesized hydrogels, prepared by dissolving 0.35 g of ACZ-SA-PEG hydrogels in 10 mL of deionized water. After rapidly stirring the mixture for 30 minutes, 10 μL of freshly prepared 1.9 M $NaBH_4$, maintained on ice, was added to the solution and stirred at RT for 1.5 hours. The resulting products were centrifuged and washed three times with deionized water, then resuspended in a 0.1% chitosan solution and stored at 4 ° C until use.

Construction of the TCPFC strategy

This TCPFC strategy combined CRISPR-mediated target recognition with RNA transcription amplification in a single reaction vessel, which was initiated by introducing the target into a unified mixture comprising Cas13a/crRNA complexes, T7 RNA polymerase, the transcriptional templates, and NTPs. The design featured an RNA-DNA hybrid molecule, composed of an RNA segment that was cleavable by Cas13a/crRNA and a DNA segment that served as the template for target transcription. Specifically, a 50 μL reaction mixture was prepared, comprising 5 μL of 10 x Cas13a buffer, 5 μL of T7 RNA Polymerase 10 x buffer, various concentrations of 2 μL of target

ARTICLE IN PRESS

miRNAs (three miRNA signatures) or extracted samples, 5 μL of 100 nM single-stranded RNA (ssRNA) reporters, 10 μL of 10 mM NTP mix, 1 μL of 50 U RNase inhibitor, 4 μL of 1 μM T7 RNA Polymerase, 4 μL of 1 μM Cas13a/crRNA, 1.6 μL of 10 μM template stands and 12.4 μL diethyl pyrocarbonate-treated water. This mixture was then placed in a 200 μL basic reaction tube and incubated at 37 °C for 60 minutes. The fluorescence signals were captured using the PCR system.

Preparation of S2-DA

The S2-DA composite was obtained as follows: Firstly, 25 μL of 100 μM RNA (UUUUU) and carboxyl-modified DNA (S2) was combined with 1 mL of PBS (0.1 M, pH 7.4), followed by the addition of 20 μL of 100 mM EDC and 5 μL of 100 mM NHS, and the mixture was stirred at 4 ° C for 2 hours to activate the carboxyl moieties on S2 stands. Subsequently, The above mixture was combined with 200 μL of 5 mM dopamine (DA) solution and continuously agitated at 4 ° C overnight to synthesize DA-S2.

Construction of the ECL biosensor

Firstly, the surface of the glassy carbon electrode (GCE) was polished on the suede skin with Al_2O_3 powder. Secondly, the 10 μL of Au@ACZ-SA-PEG hydrogels were added on the surface of the prepared GCE and baked at 37 °C for 1 hour to form a film on the electrode surface. Meanwhile, 160 μL of 30 mM tris (2-carboxyethyl) phosphine (TCEP) was combined with 40 μL of 10 μM S1, and incubated at RT for 1 hour to activate the thiol moieties on S1 stands. Next, 10 μL of activated S1 strands was anchored onto the hydrogel-modified GCE overnight at RT, whereby the free thiol groups on S1 formed covalent Au-S bonds with the Au NPs embedded within the Au@ACZ-SA-PEG hydrogels, enabling stable and oriented probe immobilization. 5 μL of the prepared DA-S2 was then deposited onto the GCE surface and incubated for 1.5 hours at RT to allow complementary hybridization with the immobilized S1 strands, forming the S1-DA-S2 structure. Subsequently, 10 μL of mixture reaction with the TCPFC strategy was added into the prepared electrode and incubated at 37 ° C for 60 minutes. Notably, the developed biosensor was rinsed with washing buffer (0.01 M PBS, pH 7.4) after each

ARTICLE IN PRESS

reaction step. Finally, the collected the ECL signals in PBS (0.1 M PBS, pH 7.4) containing 30 mM $K_2S_2O_8$. During the ECL measurement, the parameters were cohort as follows: the photomultiplier tube voltage was 700 V, the potential scan range was -2 V to 0 V, and the scan rate was 0.5 V/s.

Collection of clinical specimens

Plasma specimens were obtained at Guang'an People's Hospital under ethics committee approval (No. 2025-041), in accordance with recognized ethical principles for research involving human participants. The complete clinical cohort comprised 260 individuals organized into two independent subsets, non-overlapping subsets with no shared samples, as illustrated in the sample flow diagram.

Subset 1: RT-qPCR validation cohort (n = 40): 20 Stage III/IV NSCLC patients and 20 HCs were enrolled exclusively for RT-qPCR quantification of candidate miRNA targets and inter-platform concordance assessment between RT-qPCR and ECL measurements.

Subset 2: ECL measurement and machine learning cohort (n = 220): HCs (n = 80), Stage I/II NSCLC (n = 40), and Stage III/IV NSCLC (n = 100) patients were measured using the fabricated ECL biosensor. Prior to any model development, this cohort was partitioned 1:1 into a train set (HC: n = 40, Stage I/II: n = 20, Stage III/IV: n = 50) and a strictly held-out test set (HC: n = 40, Stage I/II: n = 20, Stage III/IV: n = 50) via stratified random sampling, preserving the original class distribution in both partitions. Clinical metadata are summarized in Supplementary Tables S8 and S9.

All plasma specimens were stored at -80 °C until analysis and processed in a blinded manner.

Machine learning modeling

The 220 sample ECL measurement and machine learning cohort was partitioned as described above (subset 2). All cross-validation procedures employed stratified k-fold partitioning to maintain consistent class proportions across folds. Z-score normalization parameters were estimated exclusively from the train set and applied identically to the test set, ensuring that no test-set statistics influenced preprocessing. Seventeen machine

ARTICLE IN PRESS

715 learning algorithms were employed: least absolute shrinkage and selection operator
716 (LASSO), Ridge regression (Ridge), Elastic Net (Enet, $\alpha = 0.5$), stepwise generalized
717 linear model (Stepglm; forward, backward, bidirectional), eXtreme Gradient Boosting
718 (XGBoost), Random Forest (RF), Partial Least Squares Regression for Generalized
719 Linear Models (plsRglm), Gradient Boosted Regression Modeling (GBM), Linear
720 Discriminant Analysis (LDA), Generalized Linear Model Boosting (glmBoost),
721 Support Vector Machine (SVM), Shrinkage Discriminant Analysis (SDA), Regularized
722 Discriminant Analysis (RDA), Classification and Regression Trees (CART), and Naive
723 Bayes. All hyperparameter optimization was performed exclusively within the train set
724 via cross-validation in Supplementary Methods and Table S10, the test set was never
725 accessed during tuning. The model achieving the highest mean AUC across three
726 pairwise comparisons (train set) was selected as the optimal diagnostic model. To
727 formally exclude overfitting and information leakage, two complementary permutation
728 tests (Y-scrambling, $n = 1{,}000$ each) and learning curves (5-fold CV $\times$ 5 repeats, train
729 proportions 20%-100%) were performed for the optimal model. The RS for each
730 individual was calculated using the optimal diagnostic model. Specifically, the RS was
731 computed as a probability-weighted sum: RS = 0 $\times$ P(HC) + 1 $\times$ P(Stage I/II) + 2
732 $\times$ P (Stage III/IV), where P(HC), P(Stage I/II), and P(Stage III/IV) denote the
733 predicted probabilities of belonging to each class, with RS $\in$ [0, 2]. A higher RS
734 reflects a greater likelihood of advanced disease.

735 **Statistical analysis**

736 Means, standard deviation (SD), and limits of detection (LOD) were computed using
737 standard formulas. Logic-Measurer is defined as a quantitative detection system which
738 utilizes logistic regression to model the calibration curve between analyte concentration
739 and signal response, facilitating the back-calculation of unknown sample
740 concentrations. Statistical analyses and data visualization were accomplished by R
741 software (version 4.5.1), GraphPad Prism (version 10.0) and Origin (version 2021).
742 Differences between the two groups were compared by unpaired Student's t-test or
743 Kruskal-Walli's test, with $p < 0.05$ considered statistically significant.

ARTICLE IN PRESS

Data availability

Data will be made available on request.

Declarations

Ethics approval and consent to participate

All human sample test were reviewed and approved by Guang'an people's Hospital with protocol approval from the hospital's ethics committee (No. 2025-041).

Consent for publication

The participant has provided consent for the submission of this research publication to the Journal of Nanobiotechnology.

Competing interests

The authors declare no competing interests.

Funding

This work was funded by the financial support from the National Natural Science Foundation of China (No. 82502846), Natural Science Foundation of Sichuan Province (No. 2025ZNSFSC1562), Health Commission of Sichuan Province Medical Science and Technology Program (No. 25QNMP119 and No. 25QNMP041), and Special Funding for Postdoctoral Research Projects in Chongqing (No. 2023CQBSHTB3028).

Acknowledgments

We thank Home for Researchers editorial team (www.homefor-researchers.com) for language editing service.

Author details

[1]Department of Laboratory Medicine, West China Hospital, Sichuan University Sichuan University West China Hospital Guang'an Hospital, Guang'an People's Hospital, Guang'an, 638000, Sichuan, PR China

[2]Key Laboratory of Clinical Laboratory Diagnostics (Ministry of Education), College of Laboratory Medicine, Chongqing Medical University, Chongqing, 400016, PR

ARTICLE IN PRESS

China

[3]Department of Laboratory Medicine, Deyang People's Hospital, Deyang, 618000, Sichuan, PR China

[4]Department of Clinical Laboratory, Suining Central Hospital, Suining, 629000, PR China

[5]Department of Cardiology, The First Affiliated Hospital of Chongqing Medical University, Chongqing Medical University, Chongqing, 400016, PR China

[6]Department of Urology, West China Hospital, Sichuan University Sichuan University West China Hospital Guang'an Hospital, Guang'an People's Hospital, Guang'an 638000, Sichuan, PR China

[7]Department of Laboratory Medicine, Chongqing Traditional Chinese Medicine Hospital, Chongqing, 400021, PR China

References

1. Bray F, Laversanne M, Sung H, Ferlay J, Siegel RL, Soerjomataram I, Jemal A. Global cancer statistics 2022: GLOBOCAN estimates of incidence and mortality worldwide for 36 cancers in 185 countries. CA. Cancer J. Clin. 2024, **74:**229-263.

2. Provencio M, Nadal E, González-Larriba JL, Martínez-Martí A, Bernabé R, Bosch-Barrera J, Casal-Rubio J, Calvo V, Insa A, Ponce S, et al. Perioperative Nivolumab and Chemotherapy in Stage III Non-Small-Cell Lung Cancer. N. Engl. J. Med. 2023, **389:**504-513.

3. Koo MM, Swann R, McPhail S, Abel GA, Elliss-Brookes L, Rubin GP, Lyratzopoulos G. Presenting symptoms of cancer and stage at diagnosis: evidence from a cross-sectional, population-based study. Lancet Oncol. 2020, **21:**73-79.

4. Henschke CI, Yip R, Shaham D, Markowitz S, Cervera Deval J, Zulueta JJ, Seijo LM, Aylesworth C, Klingler K, Andaz S, et al. A 20-year Follow-up of the International Early Lung Cancer Action Program (I-ELCAP). Radiology, 2023, **309:**e231988.

5. Dang DK, Park BH. Circulating tumor DNA: current challenges for clinical utility. J. Clin. Invest. 2022, **132**:e154941.

ARTICLE IN PRESS

6. Landon BV, Annapragada AV, Niknafs N, Velculescu VE, Anagnostou V. Liquid biopsies across the cancer care continuum. Nat. Med. 2025, **31:**4006-4021.

7. Henschke C, Huber R, Jiang L, Yang D, Cavic M, Schmidt H, Kazerooni E, Zulueta JJ, Sales Dos Santos R, Ventura L. Perspective on Management of Low-Dose Computed Tomography Findings on Low-Dose Computed Tomography Examinations for Lung Cancer Screening. From the International Association for the Study of Lung Cancer Early Detection and Screening Committee. J. Thorac. Oncol. 2024, **19:**565-580.

8. Chen CL, Hsu JS, Shen YW, Hsu CH, Kao SY, Lai WA, Chuang CH, Liu YW, Lee JY, Chou SH, et al. Changes in Staging and Management of Non-Small Cell Lung Cancer (NSCLC) Patients Following the Implementation of Low-Dose Chest Computed Tomography (LDCT) Screening at Kaohsiung Medical University Hospital. Cancers, 2024, **16:** 3727.

9. Bhamani A, Creamer A, Verghese P, Prendecki R, Horst C, Tisi S, Hall H, Khaw CR, Mullin M, McCabe J, et al. Low-dose CT for lung cancer screening in a high-risk population (SUMMIT): a prospective, longitudinal cohort study. Lancet Oncol. 2025, **26:**609-619.

10. Matrana M, Shukla V, Kingsbury D, Poliak M, Lipton J, McMillin M, Malinow LB, Venn O, Beausang JF, Stanley G, et al. Real-world data and clinical experience from over 100,000 multi-cancer early detection tests. Nat. Commun. 2025, **16:**9625.

11. Black JRM, Bartha G, Abbott CW, Boyle SM, Karasaki T, Li B, Chen R, Harris J, Veeriah S, Colopi M, et al. Ultrasensitive ctDNA detection for preoperative disease stratification in early-stage lung adenocarcinoma. Nat. Med. 2025, **31:**70-76.

12. Nikanjam M, Kato S, Kurzrock R. Liquid biopsy: current technology and clinical applications. J. Hematol. Oncol. 2022, **15:**131.

13. Vire B, Payen L, Vignault C, Hofman V, Marquette CH, Berthet JP, Boutros J, Ilie M, Penaranda G, Pourquier P, et al. The lung cancer-associated blood biomarker hPG(80) exhibits a reversible increase in response to smoking in asymptomatic

ARTICLE IN PRESS

individuals. Biomark. Res. 2025, **13:**148.

14. Wang J, Huang J, Hu Y, Guo Q, Zhang S, Tian J, Niu Y, Ji L, Xu Y, Tang P, et al. Terminal modifications independent cell-free RNA sequencing enables sensitive early cancer detection and classification. Nat. Commun. 2024, **15:**156.
15. Rasmussen M, Reddy M, Nolan R, Camunas-Soler J, Khodursky A, Scheller NM, Cantonwine DE, Engelbrechtsen L, Mi JD, Dutta A, et al. RNA profiles reveal signatures of future health and disease in pregnancy. Nature, 2022, **601:**422-427.
16. Moufarrej MN, Vorperian SK, Wong RJ, Campos AA, Quaintance CC, Sit RV, Tan M, Detweiler AM, Mekonen H, Neff NF, et al. Early prediction of preeclampsia in pregnancy with cell-free RNA. Nature, 2022, **602:**689-694.
17. Sikosek T, Horos R, Trudzinski F, Jehn J, Frank M, Rajakumar T, Klotz LV, Mercaldo N, Kahraman M, Heuvelman M, et al. Early Detection of Lung Cancer Using Small RNAs. J. Thorac. Oncol. 2023, **18:**1504-1523.
18. Pastorino U, Boeri M, Sestini S, Sabia F, Milanese G, Silva M, Suatoni P, Verri C, Cantarutti A, Sverzellati N, et al. Baseline computed tomography screening and blood microRNA predict lung cancer risk and define adequate intervals in the BioMILD trial. Ann. Oncol. 2022, **33:**395-405.
19. Nesselbush MC, Luca BA, Jeon YJ, Jabara I, Meador CB, Garofalo A, Binkley MS, Hui AB, van 't Erve I, Xu N, et al. An ultrasensitive method for detection of cell-free RNA. Nature, 2025, **641:**759-768.
20. Koch C, Reilly-O'Donnell B, Gutierrez R, Lucarelli C, Ng FS, Gorelik J, Ivanov AP, Edel JB. Nanopore sequencing of DNA-barcoded probes for highly multiplexed detection of microRNA, proteins and small biomarkers. Nat. Nanotechnol. 2023, **18:**1483-1491.
21. Ma L, Guo H, Zhao Y, Liu Z, Wang C, Bu J, Sun T, Wei J. Liquid biopsy in cancer current: status, challenges and future prospects. Signal Transduct. Target. Ther. 2024, **9:**336.
22. Meng F, Yu W, Chen C, Guo S, Tian X, Miao Y, Ma L, Zhang X, Yu Y, Huang L, et al. A Versatile Electrochemical Biosensor for the Detection of Circulating

ARTICLE IN PRESS

MicroRNA toward Non-Small Cell Lung Cancer Diagnosis. Small, 2022, **18:**e2200784.

23. Li S, Zhang H, Zhu M, Kuang Z, Li X, Xu F, Miao S, Zhang Z, Lou X, Li H, Xia F. Electrochemical Biosensors for Whole Blood Analysis: Recent Progress, Challenges, and Future Perspectives. Chem. Rev. 2023, **123:**7953-8039.
24. Zouari M, Aissaoui-Zid D, Campuzano S, Barderas R, Srairi-Abid N, Pingarrón JM, Raouafi N. Multipurpose E-bioplatform targeting Kv channels in whole cancer cells and evaluating of their potential therapeutics. Anal. Chim. Acta, 2022, **1231:**340397.
25. Zouari M, Barderas R, Pingarrón JM, Raouafi N, Campuzano S. First electrochemical bioplatform to assist in personalized 5-fluorouracil chemotherapy. Sens. Actuat. B-Chem. 2024, **401:**135017.
26. Knežević S, Han D, Liu B, Jiang D, Sojic N. Electrochemiluminescence Microscopy. Angew Chem. Int. Ed. Engl. 2024. **63:**e202407588.
27. Shen B, Li L, Liu C, Li X, Li X, Cheng X, Wu H, Yang T, Cheng W, Ding S. Mesoporous Nanozyme-Enhanced DNA Tetrahedron Electrochemiluminescent Biosensor with Three-Dimensional Walking Nanomotor-Mediated CRISPR/Cas12a for Ultrasensitive Detection of Exosomal microRNA. Anal. Chem. 2023, **95:**4486-4495.
28. Suzuki R, Iwai S, Kirino R, Sato K, Konishi M, Hasegawa G, Ishizuka N, Matsukawa K, Tanaka K, Villani E, Inagi S. An electrochemiluminescence device powered by streaming potential for the detection of amines in flowing solution. Nat. Commun. 2025, **16**:8217.
29. Duan Y, Song Y, Fan N, Yao Y, Deng S, Ding S, Shen B, Yin Q. Self-enhanced luminol-based electrochemiluminescent hydrogels: An ultrasensitive biosensing platform for fusion gene analysis coupled with target-initiated DNAzyme motor. Biosens. Bioelectron. 2022, **197:**113784.
30. Kalligosfyri PM, Scognamiglio L, Sossich E, Cheng N, Polo F, Cinti S. Exploring the Feasibility of Paper-Based Substrates for User-Friendly

ARTICLE IN PRESS

Electrochemiluminescent Sensors. Anal. Chem. 2026, **98:**3485-3492.

31. Zhou Y, Wei X, Chen J, Xiong H, Sui D, Chen X, Yang W. A Three-Dimensional Electrochemiluminescence Sensor Integrated with Peptide Hydrogel for Detection of H(2)O(2) Released from Different Subtypes of Breast Cancer Cells. Anal. Chem. 2024, **96:**13464-13472.
32. Liang W, Huang R, Li Q, Liang Y, Teng X. Hydrogel-assisted chemiluminescence and electrochemiluminescence systems for bioanalytical applications. Anal. Methods, 2025, **17:**5546-5562.
33. Zhang Y, Tan Y, Lao J, Gao H, Yu J. Hydrogels for Flexible Electronics. ACS Nano. 2023, **17:**9681-9693.
34. Zhang Y, Hu C, Yin Y, Ren K, He Y, Gao Y, Han H, Zhu C, Wang W. CRISPR/Cas12a-Responsive Smart DNA Hydrogel for Sensitive Electrochemiluminescence Detection of the Huanglongbing Outer Membrane Protein Gene. Anal. Chem. 2024, **96:**11611-11618.
35. Singh NK, Wang Y, Wen C, Davis B, Wang X, Lee K, Wang Y. High-affinity one-step aptamer selection using a non-fouling porous hydrogel. Nat. Biotechnol. 2024, **42:**1224-1231.
36. He H, Yin C, Liu Z, Wang Y, Zheng X, Zhang P, Feng Y, Geng X, Lyu J, He Q, et al. Convenient DNA Hydrogel Synthesis via Self-Templated Primer-Driven Isothermal Amplification. Adv. Mater. 2025, **38:**e11658.
37. Wang Y, Shen B, Luo N, Li C, Wu H, Wang Y, Tian S, Li X, Liu R, Li X, et al. Self-enhanced nanohydrogel electrochemiluminescence biosensor based on CRISPR/Cas12a and gold platinum nanoparticles modification for high-sensitivity detection of Burkholderia pseudomallei. Chem. Eng. J. 2024, **486:**150279.
38. Chen Y, Davidson NM, Wan YK, Yao F, Su Y, Gamaarachchi H, Sim A, Patel H, Low HM, Hendra C, et al. A systematic benchmark of Nanopore long-read RNA sequencing for transcript-level analysis in human cell lines. Nat. Methods, 2025, **22:**801-812.
39. Ren R, Cai S, Fang X, Wang X, Zhang Z, Damiani M, Hudlerova C, Rosa A, Hope

ARTICLE IN PRESS

J, Cook NJ, et al. Multiplexed detection of viral antigen and RNA using nanopore sensing and encoded molecular probes. Nat. Commun. 2023, **14:**7362.

40. de Gonzalo-Calvo D, Sopić M, Devaux Y. Methodological considerations for circulating long noncoding RNA quantification. Trends Mol. Med. 2022, **28:**616-618.

41. Reggiardo RE, Maroli SV, Peddu V, Davidson AE, Hill A, LaMontagne E, Aaraj YA, Jain M, Chan SY, Kim DH. Profiling of repetitive RNA sequences in the blood plasma of patients with cancer. Nat. Biomed. Eng. 2023, **7:**1627-1635.

42. Karimzadeh M, Momen-Roknabadi A, Cavazos TB, Fang Y, Chen NC, Multhaup M, Yen J, Ku J, Wang J, Zhao X, et al. Deep generative AI models analyzing circulating orphan non-coding RNAs enable detection of early-stage lung cancer. Nat. Commun. 2024, **15:**10090.

43. Dama E, Colangelo T, Cuttano R, Dziadziuszko R, Dandekar T, Widlak P, Rzyman W, Veronesi G, Bianchi F. A plasma 9-microRNA signature for lung cancer early detection: a multicenter analysis. Biomark. Res. 2025, **13:**74.

44. Akbarzadeh Solbu A, Koernig A, Kjesbu JS, Zaytseva-Zotova D, Sletmoen M, Strand BL. High resolution imaging of soft alginate hydrogels by atomic force microscopy. Carbohydr. Polym. 2022, **276:**118804.

45. Roh S, Jang SY, Jung Y, Lee K, Yoo J. Development of Substrate-Independent Antifouling and Bactericidal Surfaces Using Visible Light Cross-Linked Hydrogel Coatings for Biomedical Applications. Adv. Healthc. Mater. 2025, **14:**e2402565.

46. Li Y, Liu S, Zhang J, Wang Y, Lu H, Zhang Y, Song G, Niu F, Shen Y, Midgley AC, et al. Elastic porous microspheres/extracellular matrix hydrogel injectable composites releasing dual bio-factors enable tissue regeneration. Nat. Commun. 2024, **15:**1377.

47. Vinnacombe-Willson GA, Conti Y, Stefancu A, Weiss PS, Cortés E, Scarabelli L. Direct Bottom-Up In Situ Growth: A Paradigm Shift for Studies in Wet-Chemical Synthesis of Gold Nanoparticles. Chem. Rev. 2023, **123:**8488-8529.

48. El Hariri El Nokab M, Es Sayed J, De Witte F, Dewettinck K, Elshewy A, Zhang Z,

ARTICLE IN PRESS

Van Steenberge PHM, Wang T, Sebakhy KO. A comparative analytical study for the different water pools present in alginate hydrogels: Qualitative vs. quantitative approaches. Food Hydrocolloids, 2024, **154:**110159.

49. Joe A, Manivasagan P, Park JK, Han HW, Seo SH, Thambi T, Giang Phan VH, Kang SA, Conde J, Jang ES. Electric Field-Responsive Gold Nanoantennas for the Induction of a Locoregional Tumor pH Change Using Electrolytic Ablation Therapy. ACS Nano. 2024, **18:**19581-19596.
50. Lyu N, Deng D, Xiang Y, Du Z, Mou X, Ma Q, Huang N, Lu J, Li X, Yang Z, Zhang W. An insect sclerotization-inspired antifouling armor on biomedical devices combats thrombosis and embedding. Bioact. Mater. 2024, **33:**562-571.
51. Wang M, Liu Q, Li L, Wang D, Zou Y, Hu J, Xiao Y, Lan Y, Yang Y, Guo X, et al. Construction of carbazole-conjugated dual-emission fluorescent covalent organic framework for distinguishing p-nitroaniline/p-nitrophenol and adsorbing nitroanilines/nitrophenols. J. Hazard. Mater. 2025, **483:**136631.
52. Lyu Y, Becerril LM, Vanzan M, Corni S, Cattelan M, Granozzi G, Frasconi M, Rajak P, Banerjee P, Ciancio R, et al. The Interaction of Amines with Gold Nanoparticles. Adv. Mater. 2024, **36:**e2211624.
53. Lu C, Maity B, Peng X, Ito N, Abe S, Sheng X, Ueno T, Lu D. Design of a gold clustering site in an engineered apo-ferritin cage. Commun. Chem. 2022, **5:**39.
54. Lorestani F, Zhang X, Abdullah AM, Xin X, Liu Y, Rahman M, Biswas MAS, Li B, Dutta A, Niu Z, et al. A highly sensitive and long-term stable wearable patch for continuous analysis of biomarkers in sweat. Adv. Funct. Mater. 2023, **33:**2306117.
55. Kim B, Sung MC, Lee GH, Hwang B, Seo S, Seo JH, Kim DW. Aligned Ion Conduction Pathway of Polyrotaxane-Based Electrolyte with Dispersed Hydrophobic Chains for Solid-State Lithium-Oxygen Batteries. Nanomicro. Lett. 2024, **17:**31.
56. Wang G, Wang Y, Ding Y, Chen X, Li S, Zhou W, Ma R, Tang M, Shao X, Shu Z, et al. Smart Gated Hollow Mesoporous Silica Hydrogel for Targeting Endoplasmic Reticulum Stress and Promoting Periodontal Tissue Regeneration. Adv. Sci. 2025,

ARTICLE IN PRESS

12:e08400.

57. Dou T, Zhu Y, Chu Z, Sun L, Li Z, Jing L. Controlled synthesis of Au@TiO2 mesoporous hollow nanofibers by one-step polyethylenimine-regulated electrospinning method for efficiently photocatalytic oxidation of CO. Appl. Catal. B Environ. 2024, **354:**124112.

58. Gootenberg JS, Abudayyeh OO, Kellner MJ, Joung J, Collins JJ, Zhang F. Multiplexed and portable nucleic acid detection platform with Cas13, Cas12a, and Csm6. Science. 2018, **360**:439-444.

59. Song C, Li J, Wang F, Peng Z, Shen Y, Huang C, Deng S, Yang H, Yang D, Cai R, Tan W. Multifunctional AuAgPt Nanoframes for a Stimuli-Responsive Electrochemiluminescence Aptasensor. ACS Nano. 2025, **19:**26161-26169.

60. Ritchie ME, Phipson B, Wu D, Hu Y, Law CW, Shi W, Smyth GK. limma powers differential expression analyses for RNA-sequencing and microarray studies. Nucleic Acids Res. 2015, **43:**e47.

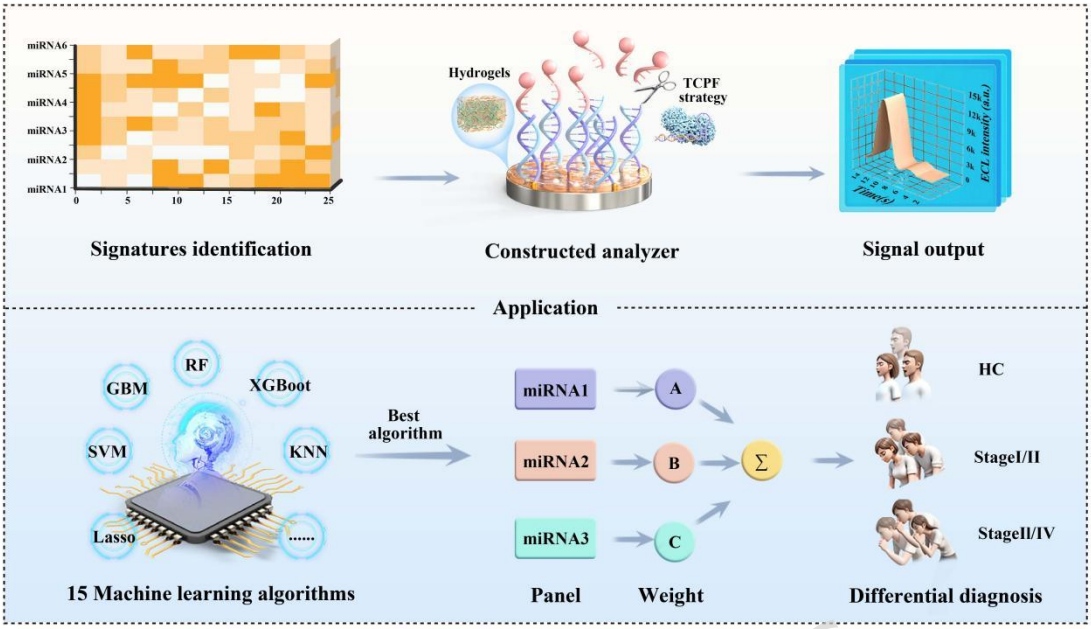
61. Liu GW, Pickett MJ, Kuosmanen JLP, Ishida K, Madani WAM, White GN, Jenkins J, Park S, Feig VR, Jimenez M, et al. Drinkable in situ-forming tough hydrogels for gastrointestinal therapeutics. Nat. Mater. 2024, **23:**1292-1299.

Supporting Information

Additional supporting information can be found online in the Supporting Information section.

ARTICLE IN PRESS

994 **Table of content (TOC)**



995

ARTICLE IN PRESS